# CHARACTERIZATION OF THE INNER KNOT OF THE CRAB: THE SITE OF THE GAMMA-RAY FLARES?

ALEXANDER RUDY[1], DIETER HORNS[2], ANDREA DELUCA[3,4], JEFFERY KOLODZIEJCZAK[5], ALLYN TENNANT[5], YAJIE YUAN[6],
ROLF BUEHLER[7], JONATHON ARONS[8], ROGER BLANDFORD[6], PATRIZIA CARAVEO[3,4], ENRICO COSTA[9], STEPHAN FUNK[6],
ELIZABETH HAYS[10], ANDREI LOBANOV[11], CLAIRE MAX[1], MICHAEL MAYER[7], ROBERTO MIGNANI[3,12], STEPHEN L. O'DELL[5],
ROGER ROMANI[6], MARCO TAVANI[3,4], AND MARTIN C. WEISSKOPF[5]

[1] Department of Astronomy & Astrophysics, University of California, Santa Cruz, CA 95064, USA
[2] Institut für Experimentalphysik, Universität Hamburg, Luruper Chaussee 149, D-22761 Hamburg, Germany
[3] INAF–IASF Milano, via E. Bassini 15, I-20133 Milano, Italy
[4] INFN Pavia, via A. Bassi 6, I-27100 Pavia, Italy
[5] NASA Marshall Space Flight Center, Astrophysics Office (ZP12), Huntsville, AL 35812, USA
[6] W. W. Hansen Experimental Physics Laboratory, Kavli Institute for Particle Astrophysics and Cosmology, Stanford University, Stanford, CA 94305, USA
[7] DESY, Platanenallee 6, D-15738 Zeuthen, Germany
[8] Astronomy Department and Theoretical Astrophysics Center, University of California, Berkeley, 601 Campbell Hall, Berkeley, CA 94720, USA
[9] INFN Roma Tor Vergata, via della Ricerca Scientifica 1, I-00133 Roma, Italy
[10] NASA Goddard Space Flight Center, Astrophysics Science Division, Greenbelt, MD 20771, USA
[11] Max-Planck-Institut für Radioastronomie, auf dem Hügel 69, D-53121 Bonn, Germany
[12] Kepler Institute of Astronomy, University of Zielona Gora, Lubuska 2, 65-265 Zielona Gora, Poland

## ABSTRACT

A particularly intriguing recent result from $\gamma$-ray astronomy missions is the detection of powerful flares from the Crab Nebula, which challenges the current understanding of pulsar wind nebulae and acceleration mechanisms. To search for the production site(s) of these flares, we conducted a multi-wavelength observing campaign using Keck, the *Hubble Space Telescope* (*HST*), and the *Chandra X-ray Observatory*. As the short timescales of the $\gamma$-ray flares ($\lesssim 1$ day) suggest a small emitting region, the Crab's inner knot (about 0.6 arcsec from the pulsar) is a candidate site for such flaring. This paper describes observations of the inner knot, seeking to understand its nature and possible relationship with $\gamma$-ray flares. Using singular-value decomposition, analysis of the *HST* images yielded results consistent with traditional methods while substantially reducing some uncertainties. These analyses show that the knot's intrinsic properties (especially size and brightness) are correlated with its (projected) separation from the pulsar. This characterization of the inner knot helps in constraining standard shock model parameters, under the assumption that the knot lies near the shocked surface. While the standard shock model gives good agreement in several respects, two puzzles persist: (a) the observed angular size of the knot relative to the pulsar–knot separation is much smaller than expected; and (b) the variable high degree of polarization (reported by others) is difficult to reconcile with a highly relativistic downstream flow. However, the IR–optical flux of the inner knot is marginally consistent with the shock accelerating most of the Nebula's optical-emitting particles.

*Key words:* ISM: jets and outflows – ISM: supernova remnants – pulsars: individual (Crab) – techniques: image processing

## 1. INTRODUCTION

The Crab pulsar and its nebula are one of the most studied targets in the sky at all wavelengths. It serves as a test bed for pulsar theories as well as, more generally, for astrophysical non-thermal processes. A very thorough review of the Crab system, including high spatial resolution observations with *Hubble Space Telescope* (*HST*) and *Chandra*, showing the complex, dynamic interaction of the pulsar wind with the surrounding medium, has been compiled by Hester (2008). A more recent review by Bühler & Blandford (2014) also includes the saga of the $\gamma$-ray flares.

A crucial question implied by the observations of the $\gamma$-ray flares is "how are the particles being accelerated to sustain the flaring behavior?" Radiating particles must have PeV energies to emit synchrotron radiation at the observed $\gamma$-ray wavelengths. A mechanism is needed that can accelerate particles to such high energies in less than one gyration time in the ambient magnetic field. For example, the large flare of 2011 April produced a radiant energy equivalent to the energy stored in the mean magnetic field within a region of order $2 \times 10^{14}$ m subtending an angle $\approx 0\rlap{.}''3$ at 2 kpc, consistent with the emission-region size estimated from light travel time arguments (Weisskopf et al. 2013).

An intense theoretical effort is underway to explain the variable Crab behaviors (e.g., Komissarov & Lyutikov 2011; Uzdensky et al. 2011; Yuan et al. 2011; Arons 2012; Bykov et al. 2012; Cerutti et al. 2012, 2013; Clausen-Brown & Lyutikov 2012; Lyubarsky 2012; Lyutikov et al. 2012; Sturrock & Aschwanden 2012; Baty et al. 2013; Teraki & Takahara 2013). However, the mechanism driving the flares, their impulsive nature, the $\approx 12$-month recurrence time, and the location remain unknown. Possible explanations include plasma instabilities in the nebula, magnetic reconnection, discontinuity in the pulsar wind acceleration, emission from the anvil, emission from the inner knot, or portions of the termination shock. See, for example, the review by Hester (2008) for the association of specific features with this nomenclature.

There are a number of reasons to suspect that the feature known as the "inner knot" should be considered as a possible site for the origin of the flares (e.g., Komissarov & Lyutikov 2011). First, the luminosity of the flares accounts for a relatively high fraction of the pulsar spin-down luminosity

(assuming a radiation efficiency of 3%–5%), suggesting an origin in a region close to the pulsar (Tavani et al. 2011). Second, the very short variability timescales combined with causality arguments, strongly constrain the size of the flare's emitting region (Striani et al. 2011; Buehler et al. 2012).

A multi-wavelength campaign to study the Crab, described in Weisskopf et al. (2013), is being performed. Another $\gamma$-ray flare—the second largest observed to date—was detected with *Fermi*/LAT in 2013 March (Mayer et al. 2013). This triggered further observations with Keck, with the *HST*, and with the *Chandra X-ray Observatory*. Here we concentrate on what was learned about the inner knot as a consequence of this campaign. We note that very-high-energy ($E \geqslant 100$ GeV) contemporaneous data from the HESS (H.E.S.S. Collaboration et al. 2014) and VERITAS (Aliu et al. 2014) Cherenkov-telescope arrays found no significant correlation of TeV flux with the flare observed with *Fermi*/LAT.

The observations are presented in Section 2. The measured properties of the knot are given in Section 3. Section 4 compares observations of the inner knot at the different wavelengths. A comparison and an examination of possible correlations of the knot's properties with $\gamma$ rays detected using the *Fermi*/LAT are discussed in Section 5. Section 6 discusses theoretical implications. Section 7 summarizes our findings.

## 2. THE OBSERVATIONS

The feature we refer to as the "inner knot" (aka "knot 1," or "synchrotron knot") was discovered by Hester et al. (1995) in a detailed study of the Crab using high-resolution images taken with *HST*. The feature, although resolved in those data, is small ($\approx 0\rlap{.}''1$) and close to the pulsar ($\approx 0\rlap{.}''6$). The feature was first suggested to be associated with a shock or instability in the jet $\approx 1500$ AU from the pulsar, due to its good alignment with the jet and elongation perpendicular to the jet. Later Komissarov & Lyubarsky (2003) proposed, based on two-dimensional (2D) magnetohydrodynamic (MHD) simulations of the pulsar wind nebula, that the knot represents Doppler-boosted emission from an oblique termination shock. Synthetic synchrotron images from these 2D simulations (Komissarov & Lyutikov 2011), and more recently three-dimensional (3D) simulations (Porth et al. 2014), indeed show a knot-like feature when the system is viewed from the proper (and reasonable) orientation. Moreover, the observed high degree of polarization and a position angle aligned with the symmetry axis (Moran et al. 2013) seems to lend further support to the oblique shock scenario.

The salient features of the inner knot deduced prior to our observations indicate that it has a power-law spectrum $F_\nu \propto \nu^{-\alpha}$ with index $\alpha \sim 0.8$ in the IR to optical (Sollerman 2003; Melatos et al. 2005) and, as most recently measured by Moran et al. (2013), the flux varies, the position appears to change, the degree of polarization is very large but does not appear to change with the flux (but see the discussion at the end of Section 5), and the magnetic field (determined from the position angle of the optical polarization) is orthogonal to the axis of symmetry (presumably the spin axis) and consistent with the direction of the field for the rest of the inner nebula.

### 2.1. Keck

We obtained $K'$- and $H$-band near-infrared (NIR) images of the inner $40''$ of the Crab Nebula using the Keck Near-infrared

**Table 1**
Summary of the 12 Keck Observations

| # | Date | MJD[a] | Instrument[b] | Exposure (s) |
|---|------|-----|------------|--------------|
| K1 | 2012 Feb 08 | 55965.285 | NIRC2-wide | 420 |
| K2 | 2012 Mar 05 | 55991.319 | NIRC2-wide | 420 |
| K3 | 2012 Dec 22 | 56283.408 | NIRC2-wide | 1250 |
| K4 | 2012 Dec 23 | 56284.410 | NIRC2-narrow | 870 |
| K5 | 2012 Dec 24 | 56285.388 | NIRC2-narrow | 1350 |
| K6 | 2012 Dec 25 | 56286.390 | NIRC2-wide | 1125 |
| K7 | 2013 Feb 06 | 56329.308 | NIRC2-narrow | 2020 |
| K8 | 2013 Oct 22 | 56587.448 | NIRC2-narrow | 640 |
| K9 | 2014 Jan 09 | 56666.274 | NIRC2-wide | 1560 |
| K10 | 2014 Jan 09 | 56666.377 | NIRC2-narrow | 2580 |
| K11 | 2014 Jan 17 | 56674.325 | NIRC2-wide | 2270 |
| K12 | 2014 Jan 17 | 56674.394 | NIRC2-narrow | 1260 |

**Notes.**
[a] Quoted MJD is at the midpoint of the observation.
[b] Plate scale is $0\rlap{.}''04$/pixel for NIRC2-wide; $0\rlap{.}''01$/pixel for NIRC2-narrow.

Camera 2 (NIRC2; K. Matthews, PI), with laser guide star adaptive optics (AO; Wizinowich et al. 2006). From 2012 February to 2014 January, we obtained 11 observations of the nebula during $\gamma$-ray quiescent periods and 1 target-of-opportunity observation (K8) triggered by $\gamma$-ray flares. Table 1 summarizes the Keck observations.

Data reduction was carried out using the pipeline developed by Ghez et al. (2008). Individual frames were sky-subtracted, flat-fielded, bad-pixel-corrected, and corrected for the NIRC2's camera distortion. We used the solution developed by Yelda et al. (2010), which matched the positions of stars in the globular cluster M92 measured with *HST* to those measured in the NIRC2. Frames were checked to ensure that they showed no irregularities in the point-spread function (PSF), and that the Strehl ratio was at least $\sim 0.10$. Individual frames were then combined using the Drizzle algorithm (Fruchter & Hook 2002) to provide sub-pixel accuracy and high signal-to-noise images for analysis and modeling (Section 3.1 and Appendix).

The observations were conducted with two different pixel scales, using the NIRC2 "wide" camera, with $0\rlap{.}''04$ pixels and a $40'' \times 40''$ field of view, and the NIRC2 "narrow" camera, with $0\rlap{.}''01$ pixels and a $10'' \times 10''$ field of view. The total effective exposure times ranged from 420 to $\approx 2600$ s. The shorter exposures result in optimal use of 1-hr Target-of-opportunity interrupts—including acquisition, calibration, and sky measurements.

The spatial resolution of Keck's NIRC2 with AO proved to be very effective for resolving the detailed structure and position of the knot. Figure 1 shows the 12 NIRC2 images. In the narrow camera, the center of the pulsar and the center of the knot are separated by $\approx 60$ pixels. Typical values for the signal-to-noise ratio of the knot are 5. The PSF of NIRC2 with AO varies slightly in time due to the variable performance of the AO system. As the pulsar and knot are well-resolved from each other in the Keck images, we chose not to deconvolve the PSF from the Keck images.

### 2.2. HST

Since 2012 January, we have obtained 22 observations using the *HST* Advanced Camera for Surveys (ACS) Wide-field Channel (WFC), with $0\rlap{.}''05$ pixels. Each observation comprises four exposures totaling 2000 s and uses a standard 4-point
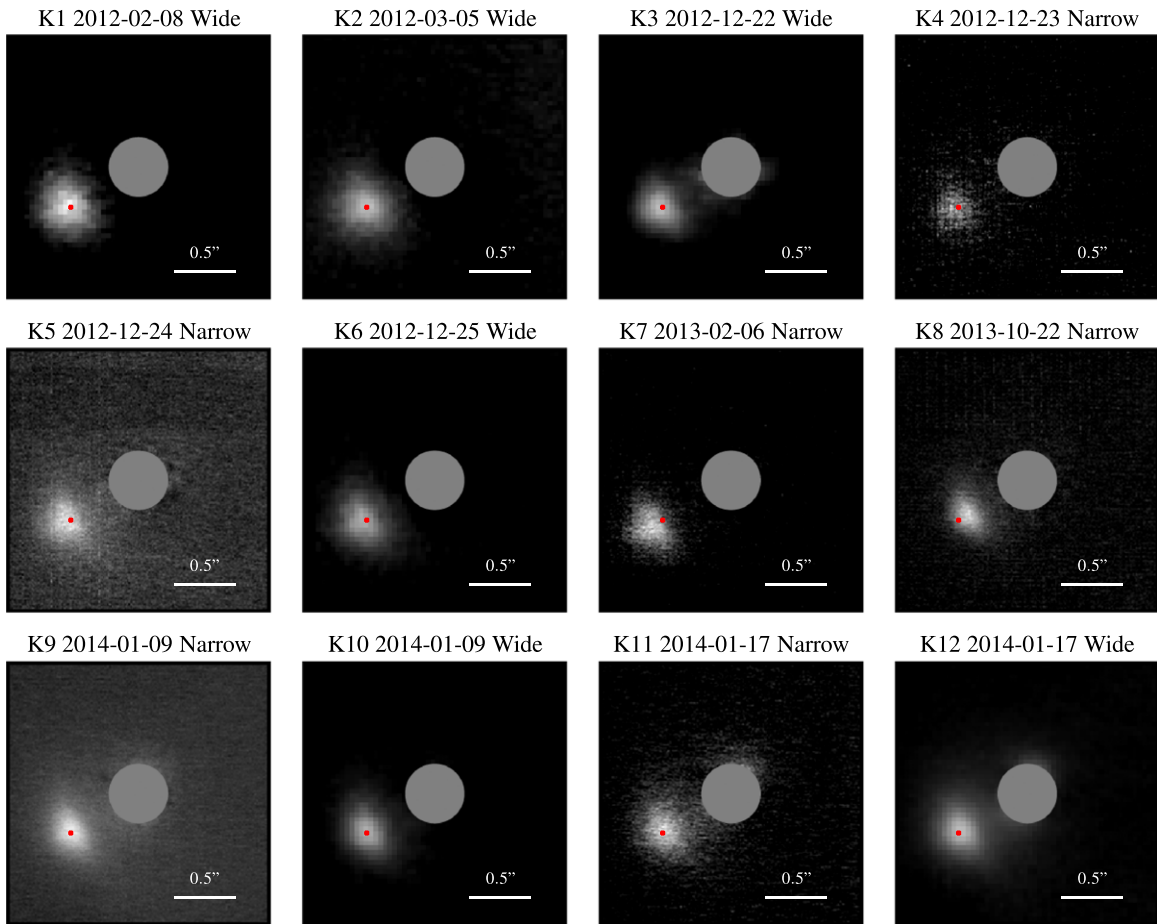
**Figure 1.** Individual images of the inner knot, with the pulsar removed, from Keck NIRC2 with laser guide star adaptive optics (AO). In each image, the PSF of the pulsar has been subtracted using the scaled PSF of a nearby star and replaced with a gray circle at the original location of the pulsar. Each image is $2\rlap{.}''2$ by $2\rlap{.}''2$. The images are from the NIRC2-wide camera ($0\rlap{.}''04$ pixels) or the NIRC2-narrow camera ($0\rlap{.}''01$ pixels). All images were taken using the $K'$ filter. For positional reference, the red dot marks the average position of the inner knot across all 12 observations.

BOX dithering pattern to fill the inter-chip gap as well as to allow efficient cosmic ray cleaning. We employed the $F550M$ filter, which is well-suited to sampling continuum emission from the Crab with almost no contamination from line emission.

Table 2 summarizes the observations, listing the date and the mean observing time. The Appendix discusses in detail our analyses of the 22 $HST$/ACS images. Figure 2 displays the processed images, in which we have removed the effects of the $HST$/ACS WFC PSF using singular-value decomposition (SVD) and Richardson–Lucy deconvolution.

### 2.3. Chandra

Our approach for searching for X-ray emission from the inner knot with *Chandra* involved a special use of both the high time resolution and high spatial resolution of the High-resolution Camera for Spectroscopy (HRC-S) array in timing mode. This approach combines the best spatial resolution and the best time resolution afforded by the *Chandra* instrumentation. To achieve the time resolution, it is vital that the counting rate be below the rate where telemetry is saturated (see, e.g., Tennant et al. 2001). Consequently, the Low-energy Transmission Grating was inserted into the optical path to reduce the flux. As inserting the grating is of itself insufficient to avoid telemetry saturation, the trigger threshold of the HRC-S was raised to reduce the rate of detected events. This approach was first successfully used in a trial experiment (ObsID 11245) on 2010 November 16.

The next set of observations in this mode was initiated by us on 2013 March 5 as part of a sequence triggered by a $\gamma$-ray flare (Ojha et al. 2013). Unfortunately, the gain of the HRC had dropped since 2010. Consequently, the trigger threshold was too high during our first observation on March 5–6, reducing the counting rate from the pulsar to about a quarter of that expected, dramatically decreasing the number of detected counts. The next HRC observation was to take place on March 10 and the observation had already been fully planned with the commands to execute on board the spacecraft. To replan at this stage would require an extremely short turnaround, yet it was accomplished. Finally, beginning on 2013 October 22, we triggered another sequence of HRC observations in response to the announcement of another $\gamma$-ray flare (Buson et al. 2013).

We also consider ObsID 9765, taken on 2008 January 22. For this observation the HRC was operated in a more standard configuration with the threshold set at the nominal value. However, to reduce the count rate, a blade was inserted into the optical path, which is no longer allowed. This blade also reduced the diffracted flux in one direction. By chance, this reduction is greatest near the nominal location of the knot. This reduction, together with a long integration time for this observation, results in ObsID 9765 providing the best data

**Table 2**
Summary of the 22 *HST* Observations

| # | Date | MJD[a,b] |
|---|------|------|
| H1 | 2012 Jan 08 | 55934.797 |
| H2 | 2012 Feb 10 | 55967.170 |
| H3 | 2012 Mar 12 | 55998.414 |
| H4 | 2012 Apr 22 | 56039.850 |
| H5 | 2012 Aug 16 | 56155.336 |
| H6 | 2012 Sep 10 | 56180.960 |
| H7 | 2013 Jan 10 | 56302.992 |
| H8 | 2013 Feb 24 | 56347.055 |
| H9 | 2013 Mar 06 | 56357.023 |
| H10 | 2013 Apr 01 | 56383.320 |
| H11 | 2013 Apr 14 | 56396.113 |
| H12 | 2013 Aug 13 | 56517.710 |
| H13 | 2013 Oct 20 | 56585.793 |
| H14 | 2013 Oct 29 | 56594.700 |
| H15 | 2013 Dec 01 | 56627.273 |
| H16 | 2014 Jan 20 | 56677.530 |
| H17 | 2014 Apr 13 | 56760.900 |
| H18 | 2014 Aug 10 | 56879.375 |
| H19 | 2014 Aug 21 | 56890.094 |
| H20 | 2014 Nov 16 | 56977.820 |
| H21 | 2015 Jan 21 | 57043.620 |
| H22 | 2015 Apr 16 | 57128.670 |

**Notes.**
[a] Quoted MJD is at the midpoint of the observation.
[b] Plate scale is $0''05$/pixels.

for study of the knot. Table 3 summarizes the relevant *Chandra* observations.

## 3. PROPERTIES OF THE KNOT

Each Keck (Figure 1) or *HST* (Figure 2) image obtained in this campaign clearly shows the inner knot at nominally $0''65$ southeast of the pulsar. As already noted in previous *HST* observations (Hester et al. 1995; Hester 2008; Moran et al. 2013), this feature is persistent but not static.

Here we report on our analysis of the Keck (Section 3.1) and *HST* (Section 3.2) images to measure the properties of the inner knot, changes with time, and correlations of intrinsic properties with the pulsar–knot separation. Figure 3 defines the lowest-order geometric properties of the knot: $r_0$, the projected separation of the knot's center from the pulsar; $\psi_0$, the position angle (east of north) on the sky from the pulsar to the knot's center; FWHM$_r$ and FWHM$_t$, the full widths at half maximum of the knot in the radial and tangential directions, respectively.

### 3.1. Keck

Table 4 lists the best-fit values of the model parameters for the inner knot for each of the 12 Keck observations based upon the analysis and modeling described in the Appendix. Besides listing the geometric properties ($r_0$, $\psi_0$, FWHM$_r$, and FWHM$_t$), the table lists $F_k/F_p$, the ratio of the flux in the knot to that in the pulsar. We tabulate the flux ratio rather than an absolute flux because the measured fluxes of five stars in the NIRC2-wide camera's field differed from one observation to the next. This occurs because the nebular background varies spatially across the detector in a non-trivial way, making it difficult to precisely determine the flux of any given source. Figure 4 plots

$\psi_0$, FWHM$_r$, and FWHM$_t$, and $F_k/F_p$ against $r_0$ for the Keck data.

We test for a possible correlation of each property $p$ with separation $r_0$ from the pulsar, of the form $p(r_0) = p(r_1)[r_0/r_1]^q$, where reference separation $r_1$ is the geometric average of the 12 Keck measurements. We fit the position angle of the knot, $\psi_0$, to the linear regression $\psi_0 = \psi_0(\langle r_0 \rangle) + \psi_0'(\langle r_0 \rangle)[r_0 - \langle r_0 \rangle]$, where $\langle r_0 \rangle$ is the arithmetic average. Table 5 tabulates the results of the regression analyses of the inner knot's intrinsic properties with its (projected) separation from the pulsar. Based upon the F-test probability, the power-law regression analysis finds marginally significant correlations of the radial width, tangential width, and peak intensity (surface brightness) with separation. The correlations to the separation of the knot's flux and position angle are not significant.

### 3.2. HST

Table 6 lists the best-fit values of the model parameters for the inner knot for each of the 22 *HST* observations based upon the modeling and analysis described in the Appendix. Besides listing the geometric properties ($r_0$, $\psi_0$, FWHM$_r$, and FWHM$_t$), the table lists $F_k/F_p$, the ratio of the flux in the knot to that in the pulsar, and $S_k/F_p$, the peak surface brightness scaled to the pulsar flux. Although we expected the pulsar flux to be steady, we measured small ($2.5 - \sigma$) variations and thus decided to work with the flux ratio $F_k/F_p$.

In the Appendix we discuss two ways of analyzing the *HST* data. Table 6 presents the results for one of these methods. However, our general conclusions concerning the knot's optical properties are for the most part the same for either analysis. Figure 5 plots the knot properties versus the pulsar–knot separation, based upon the *HST* data.

As with the Keck data, we perform a regression analysis of each property $p$ with separation $r_0$. (Table 7). Similarly, $r_1$ is the geometric average of the 22 *HST* observations; $\langle r_0 \rangle$, the arithmetic average.

Based upon the F-test probability, the power-law regression analysis finds statistically significant correlations of the tangential width FWHM$_t$ with separation $r_0$ from the pulsar, as well as the previously known (Moran et al. 2013) anti-correlations of flux $F_k$ and of peak surface brightness $S_k$ with separation. The correlations of radial width FWHM$_r$ and of position angle $\psi_0$ with separation $r_0$ are less strong. We note that we find similar correlations—except for the flux—using the more traditional *HST* analysis methods described in the Appendix.

### 3.3. Chandra

For the *Chandra* data, the main question is whether X-ray emission from the knot can be detected—especially in the vicinity of the bright, X-ray-emitting pulsar. The answer, unfortunately, is "No" and here we set an informative upper limit to the X-ray flux of the inner knot relative to that of the pulsar.

Table 8 shows the number of counts in each of three extraction regions: (1) centered on the approximate location of the optical knot, (2) centered on the pulsar, and (3) placed on a reference region to estimate the background. Details may be found in the Appendix and are illustrated in Figure 6. The analysis was performed both for the full phase-averaged data and for the data at pulse minimum. Consider, for example, the
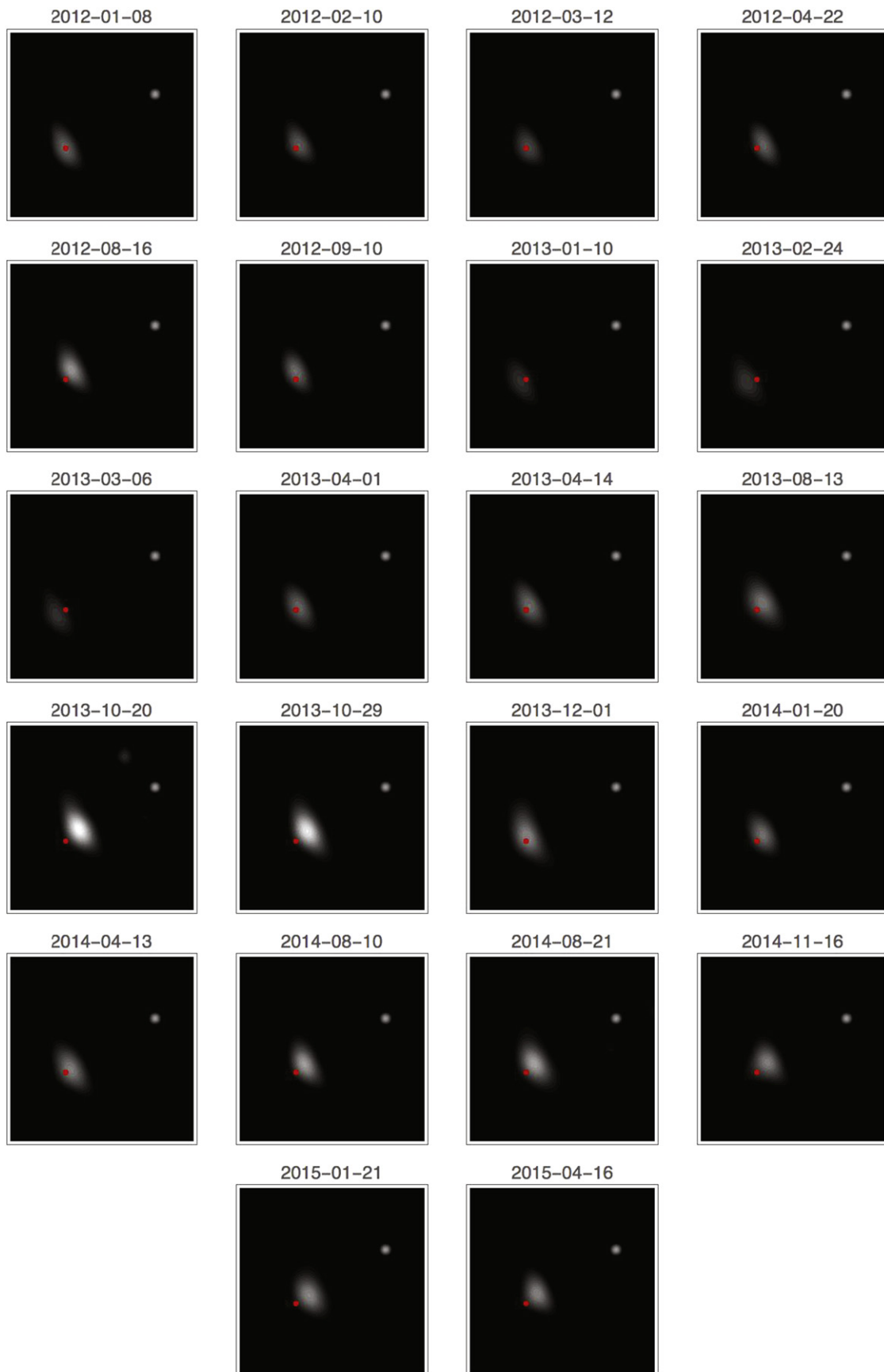
**Figure 2.** *HST*-SVD-processed images of the Crab pulsar and inner knot after removing the effects of the *HST*/ACS WFC point-spread function. For positional reference, the red dot in each image marks the position of the inner knot during the first of these 22 observations. The *HST* observations of 2013 March 06 (H9) and of 2013 October 29 (H14) each occurred at the peak of a γ-ray flare (Figure 8).

**Table 3**
Summary of the *Chandra* Observations

| # | ObsID | Date | MJD[a] | Exposure (s) |
|---|---|---|---|---|
| C1 | 09765 | 2008 Jan 22 | 54487.670 | 95082 |
| C2 | 11245 | 2010 Nov 16 | 55516.294 | 22039 |
| C3 | 14684 | 2013 Mar 05 | 56356.972 | 19485 |
| C4 | 14686 | 2013 Mar 10 | 56361.338 | 20052 |
| C5 | 14687 | 2013 Mar 17 | 56368.324 | 16718 |
| C6 | 16244 | 2013 Oct 19 | 56584.658 | 20048 |
| C7 | 16246 | 2013 Oct 22 | 56587.515 | 20013 |
| C8 | 16247 | 2013 Oct 24 | 56589.007 | 19770 |

**Note.**
[a] Quoted MJD is at the start of the observation.

phase-averaged data for ObsID 11245. Comparing the inner knot counts to the background (Table 8) we find an excess of 167 counts. If the excess were really due to the knot, we would accordingly expect an excess of 50 ($=167 \times 0.3$) counts at phase minimum. As this was not the case, we attribute the excess to the wings of the PSF from the pulsar and posit that it is due to the spring/fall asymmetry discussed in the Appendix. As the impact of that asymmetry is below the statistical noise for the data taken at phase minimum, we then use the phase minimum data to derive upper limits. We convert our phase minimum upper limit into a phase-averaged upper limit by accounting for the 0.3 phase duration of the minimum and then divide by the phase average pulsar flux. The results are listed in the last column in Table 8.

## 4. COMPARISON AMONG OBSERVATIONS OF THE INNER KNOT

Our *Chandra* observations were unable to detect X-ray flux from the knot, setting a $3\sigma$ upper limit to the ratio of knot flux to pulsar flux $F_k/F_p < 0.0022$. This upper limit is 20–40 times smaller than the ratio measured in the optical ($F_k/F_p = 0.044 \pm 0.001$) and in the near-IR ($F_k/F_p = 0.063 \pm 0.003$), indicating that the optical–X-ray spectral index of the knot is significantly steeper (by at least 0.5) than that of the pulsar.

Both our infrared and optical observations detected time variability in the pulsar–knot separation, with roughly consistent separations when measured contemporaneously (see the lower portion of Figure 7). Correlations of knot properties with pulsar–knot separation are very strong for the optical measurements but rather weak for the infrared measurements. We attribute this difference to a combination of factors—including poorer statistics for the much shorter NIR measurements and a number of systematic effects, resulting in part from the NIR PSF and background varying across the field and in time. As the lower portion of Figure 7 and Table 4 indicate, NIR-measured separations at essentially the same epoch exhibit a scatter that is substantially larger than the quoted statistical errors in the measurement, thus suggesting the presence of unaccounted systematic errors.

## 5. COMPARISON WITH $\gamma$-RAY FLUXES

It is clear from the previous sections that the intrinsic properties of the optical knot are correlated with its projected separation from the pulsar. The correlation for the NIR knot is but marginally significant. Thus, in searching for any relationship between the knot and the $\gamma$-ray flux, we concentrate on the
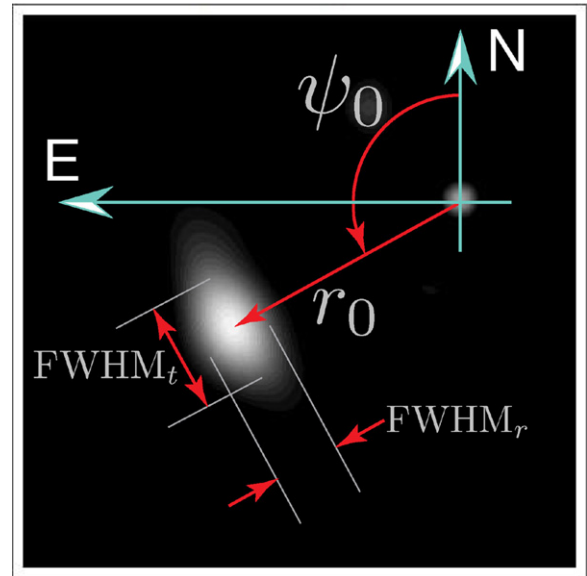


**Figure 3.** Geometric properties of the inner knot: $r_0$, the projected separation of the knot from the pulsar; $\psi_0$, the position angle (east of north) on the sky of the pulsar–knot separation; $FWHM_r$, the full width at half maximum of the knot in the radial direction; and $FWHM_t$, the FWHM of the knot in the tangential direction. The underlying image is from the 2013 October 20 *HST* observation (H13), which exhibits the minimum separation and maximum optical flux observed during this campaign.

pulsar–knot separation versus the $\gamma$-ray flux. The analysis performed to reduce the *Fermi*/LAT data is the same as that described in Mayer et al. (2013).

Table 9 lists the dates and separations measured in the Keck and in the *HST* observations, followed by the corresponding 12-hr-average *Fermi*/LAT $\geqslant 100$ MeV fluxes. The upper portion of Figure 7 shows the *Fermi*/LAT flux as a function of time covering the interval when our Keck and *HST* observations were made. The vertical lines identify times when observations were made with Keck (red) or with *HST* (green). The lower portion of Figure 7 plots the pulsar–knot separations on the same timescale. Figure 8 expands Figure 7 at the times of the three largest $\gamma$-ray flaring episodes during our observational campaign. Note that the *HST* observations of 2013 March 06 (H9) and of 2013 October 29 (H14) each fortuitously occurred within the peak of a $\gamma$-ray flare.

Interestingly, a comparison of the $\gamma$-ray light curve with the time series of pulsar–knot separations (Figure 7) finds that the most energetic $\gamma$-ray flare (2013 March) during the observational campaign occurred near the time of the greatest pulsar–knot separation. Curiously, however, this comparison also finds that the second most energetic flaring episode (2013 October) occurred near the time of the least pulsar–knot separation. The third most energetic flaring episode (2014 August) took place while the separation was midway between the average and minimum measured during the campaign. The inner knot's excursion near the 2013 March $\gamma$-ray flare and its incursion near the 2013 October flare were transient, with timescales of a few weeks—significantly longer than the time scale of a few days (or less) of a $\gamma$-ray flare. The lesser incursion of the knot near the 2014 August flaring episode was even slower.

As the timescales for motion of the inner knot appear to be an order of magnitude longer than those for the $\gamma$-ray flaring, there can be no simple correlation of $\gamma$-ray flux with pulsar–

**Table 4**
Knot Properties Based upon Analysis of the Keck Data

| # | $r_0$ | $\psi_0$ | $\mathrm{FWHM}_r$ | $\mathrm{FWHM}_t$ | $\dfrac{F_k}{F_p}$ |
|---|---|---|---|---|---|
| | $''$ | $\circ$ | $''$ | $''$ | |
| K1 | $0.6711 \pm 0.0015$ | $118.50 \pm 0.16$ | $0.3931 \pm 0.0040$ | $0.4719 \pm 0.0051$ | $0.0639 \pm 0.0045$ |
| K2 | $0.6577 \pm 0.0015$ | $121.00 \pm 0.13$ | $0.4121 \pm 0.0035$ | $0.4252 \pm 0.0042$ | $0.0626 \pm 0.0067$ |
| K3 | $0.6893 \pm 0.0011$ | $122.64 \pm 0.11$ | $0.3215 \pm 0.0028$ | $0.3948 \pm 0.0039$ | $0.0804 \pm 0.0074$ |
| K4 | $0.7118 \pm 0.0021$ | $120.96 \pm 0.18$ | $0.3401 \pm 0.0051$ | $0.4081 \pm 0.0059$ | $0.0473 \pm 0.0003$ |
| K5 | $0.6981 \pm 0.0007$ | $121.20 \pm 0.07$ | $0.2983 \pm 0.0019$ | $0.3767 \pm 0.0024$ | $0.0555 \pm 0.0005$ |
| K6 | $0.7164 \pm 0.0010$ | $120.79 \pm 0.12$ | $0.3375 \pm 0.0029$ | $0.4238 \pm 0.0042$ | $0.0599 \pm 0.0085$ |
| K7 | $0.7756 \pm 0.0013$ | $121.93 \pm 0.12$ | $0.3355 \pm 0.0034$ | $0.4049 \pm 0.0038$ | $0.0662 \pm 0.0004$ |
| K8 | $0.5722 \pm 0.0004$ | $120.33 \pm 0.06$ | $0.2216 \pm 0.0011$ | $0.3172 \pm 0.0015$ | $0.0621 \pm 0.0005$ |
| K9 | $0.6543 \pm 0.0006$ | $121.46 \pm 0.08$ | $0.2958 \pm 0.0018$ | $0.4030 \pm 0.0024$ | $0.0708 \pm 0.0047$ |
| K10 | $0.6257 \pm 0.0003$ | $115.77 \pm 0.03$ | $0.2689 \pm 0.0007$ | $0.3683 \pm 0.0009$ | $0.0663 \pm 0.0006$ |
| K11 | $0.6371 \pm 0.0008$ | $121.49 \pm 0.10$ | $0.3119 \pm 0.0022$ | $0.3787 \pm 0.0029$ | $0.0647 \pm 0.0078$ |
| K12 | $0.6438 \pm 0.0009$ | $118.99 \pm 0.09$ | $0.3248 \pm 0.0023$ | $0.3766 \pm 0.0025$ | $0.0574 \pm 0.0001$ |
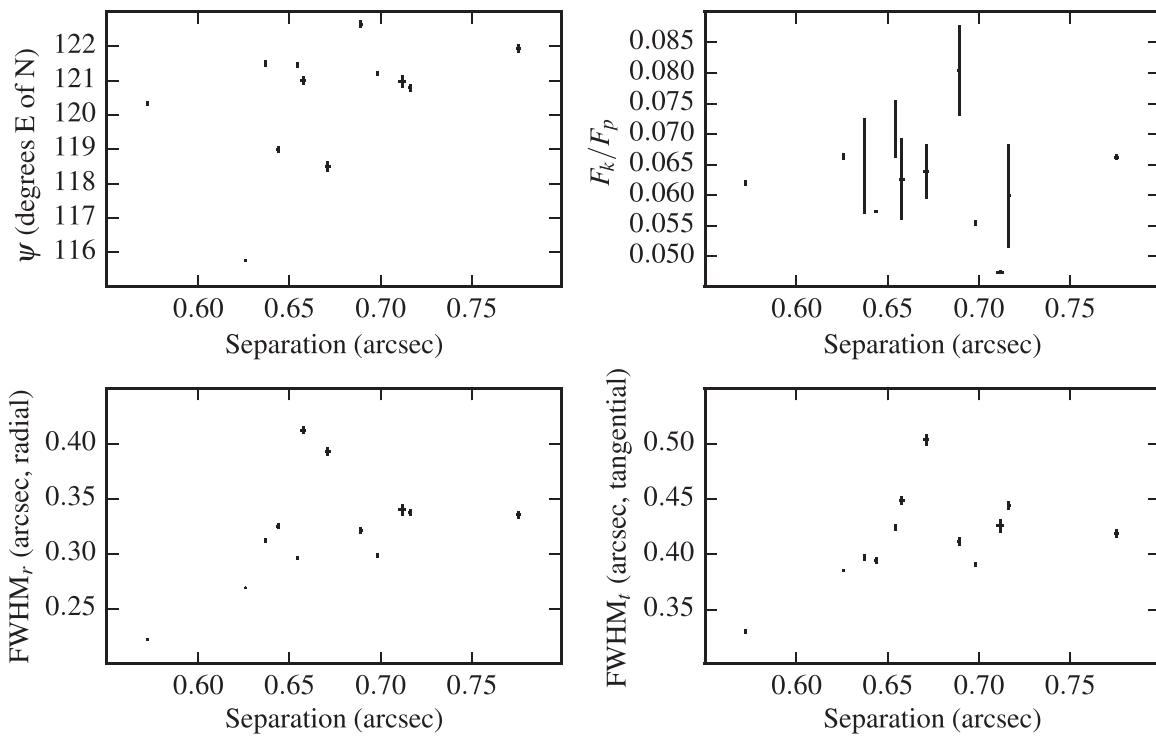


**Figure 4.** Variation of the Keck-measured knot properties vs. separation of the inner knot from the pulsar.

**Table 5**
Results of Regression Analyses for the 12 Keck Observations

Power-law for $r_1 = 0\!''6692$

| Property | Unit | $p(r_1)$ | Power-law Index $q$ | Probability |
|---|---|---|---|---|
| $\mathrm{FWHM}_r$ | $''$ | $0.3180 \pm 0.0132$ | $1.19 \pm 0.54$ | 5.4E-2 |
| $\mathrm{FWHM}_t$ | $''$ | $0.3941 \pm 0.0093$ | $0.75 \pm 0.31$ | 3.8E-2 |
| $S_k$ | $F_p/('')^2$ | $0.439 \pm 0.033$ | $-2.14 \pm 0.97$ | 5.2E-2 |
| $F_k$ | $F_p$ | $0.0626 \pm 0.0025$ | $-0.20 \pm 0.53$ | 7.1E-1 |

Linear for $\langle r_0 \rangle = 0\!''6711$

| Property | | $\psi_0(\langle r_0 \rangle)$ | $d\psi_0/dr_0$ | |
|---|---|---|---|---|
| $\psi_0$ | $\circ, \circ/''$ | $120.42 \pm 0.51$ | $15.2 \pm 10.2$ | 1.7E-1 |

**Table 6**
Knot Properties Based upon SVD Analysis of the 22 *HST* Observations (See the Appendix)

| # | $r_0$ " | $\psi_0$ ° | FWHM$_r$ " | FWHM$_t$ " | $S_k$ e/s/(")$^2$ | $F_k$ e/s | $F_p$ e/s | $\frac{F_k}{F_p}$ |
|---|---|---|---|---|---|---|---|---|
| H1 | $0.6819 \pm 0.0023$ | $120.54 \pm 0.40$ | $0.1526 \pm 0.0056$ | $0.3221 \pm 0.0116$ | $1064 \pm 33$ | $59.8 \pm 3.6$ | $1425 \pm 82$ | $0.0420 \pm 0.0035$ |
| H2 | $0.6535 \pm 0.0024$ | $119.45 \pm 0.41$ | $0.1536 \pm 0.0058$ | $0.3071 \pm 0.0114$ | $1008 \pm 32$ | $53.8 \pm 3.4$ | $1433 \pm 80$ | $0.0375 \pm 0.0032$ |
| H3 | $0.6708 \pm 0.0022$ | $120.37 \pm 0.33$ | $0.1751 \pm 0.0052$ | $0.3121 \pm 0.0092$ | $902 \pm 23$ | $55.0 \pm 2.6$ | $1471 \pm 64$ | $0.0374 \pm 0.0024$ |
| H4 | $0.6356 \pm 0.0024$ | $121.74 \pm 0.41$ | $0.1465 \pm 0.0056$ | $0.2942 \pm 0.0110$ | $1053 \pm 34$ | $52.3 \pm 3.2$ | $1276 \pm 80$ | $0.0410 \pm 0.0035$ |
| H5 | $0.6166 \pm 0.0020$ | $117.90 \pm 0.39$ | $0.1406 \pm 0.0048$ | $0.3043 \pm 0.0102$ | $1256 \pm 36$ | $61.1 \pm 3.4$ | $1231 \pm 84$ | $0.0497 \pm 0.0044$ |
| H6 | $0.6577 \pm 0.0024$ | $117.62 \pm 0.41$ | $0.1456 \pm 0.0058$ | $0.3029 \pm 0.0112$ | $1102 \pm 36$ | $56.7 \pm 3.5$ | $1184 \pm 86$ | $0.0479 \pm 0.0046$ |
| H7 | $0.7240 \pm 0.0035$ | $121.17 \pm 0.59$ | $0.1704 \pm 0.0084$ | $0.3539 \pm 0.0176$ | $675 \pm 28$ | $44.7 \pm 3.9$ | $1422 \pm 77$ | $0.0314 \pm 0.0032$ |
| H8 | $0.7516 \pm 0.0031$ | $119.91 \pm 0.50$ | $0.1751 \pm 0.0076$ | $0.3533 \pm 0.0158$ | $667 \pm 25$ | $44.5 \pm 3.4$ | $1421 \pm 65$ | $0.0313 \pm 0.0028$ |
| H9 | $0.7491 \pm 0.0033$ | $120.88 \pm 0.52$ | $0.1740 \pm 0.0080$ | $0.3362 \pm 0.0166$ | $728 \pm 29$ | $45.8 \pm 3.8$ | $1359 \pm 73$ | $0.0337 \pm 0.0033$ |
| H10 | $0.6614 \pm 0.0019$ | $120.60 \pm 0.32$ | $0.1598 \pm 0.0046$ | $0.3139 \pm 0.0090$ | $1098 \pm 27$ | $63.3 \pm 3.0$ | $1295 \pm 72$ | $0.0489 \pm 0.0036$ |
| H11 | $0.6557 \pm 0.0021$ | $119.39 \pm 0.36$ | $0.1639 \pm 0.0050$ | $0.3220 \pm 0.0098$ | $1090 \pm 28$ | $64.9 \pm 3.3$ | $1509 \pm 77$ | $0.0430 \pm 0.0031$ |
| H12 | $0.6324 \pm 0.0023$ | $119.28 \pm 0.41$ | $0.1691 \pm 0.0056$ | $0.3299 \pm 0.0110$ | $1028 \pm 29$ | $63.4 \pm 3.6$ | $1283 \pm 83$ | $0.0494 \pm 0.0042$ |
| H13 | $0.5687 \pm 0.0019$ | $117.85 \pm 0.36$ | $0.1426 \pm 0.0046$ | $0.2739 \pm 0.0082$ | $1668 \pm 44$ | $75.6 \pm 3.8$ | $1222 \pm 106$ | $0.0618 \pm 0.0062$ |
| H14 | $0.5849 \pm 0.0022$ | $118.82 \pm 0.41$ | $0.1441 \pm 0.0052$ | $0.2886 \pm 0.0098$ | $1583 \pm 48$ | $75.6 \pm 4.4$ | $1285 \pm 118$ | $0.0589 \pm 0.0064$ |
| H15 | $0.6624 \pm 0.0026$ | $118.59 \pm 0.52$ | $0.1476 \pm 0.0061$ | $0.3393 \pm 0.0144$ | $1105 \pm 40$ | $61.8 \pm 4.4$ | $1353 \pm 100$ | $0.0457 \pm 0.0047$ |
| H16 | $0.6299 \pm 0.0026$ | $118.82 \pm 0.41$ | $0.1640 \pm 0.0064$ | $0.2961 \pm 0.0106$ | $1084 \pm 35$ | $62.1 \pm 3.7$ | $1419 \pm 98$ | $0.0438 \pm 0.0040$ |
| H17 | $0.6448 \pm 0.0024$ | $120.88 \pm 0.41$ | $0.1611 \pm 0.0059$ | $0.3212 \pm 0.0109$ | $1164 \pm 35$ | $69.6 \pm 4.0$ | $1177 \pm 99$ | $0.0591 \pm 0.0060$ |
| H18 | $0.6063 \pm 0.0022$ | $119.62 \pm 0.39$ | $0.1481 \pm 0.0053$ | $0.2921 \pm 0.0097$ | $1289 \pm 38$ | $67.1 \pm 3.6$ | $1305 \pm 96$ | $0.0514 \pm 0.0055$ |
| H19 | $0.6106 \pm 0.0023$ | $118.99 \pm 0.38$ | $0.1498 \pm 0.0055$ | $0.2855 \pm 0.0098$ | $1200 \pm 36$ | $61.9 \pm 3.4$ | $1252 \pm 90$ | $0.0494 \pm 0.0052$ |
| H20 | $0.6004 \pm 0.0029$ | $119.39 \pm 0.44$ | $0.1827 \pm 0.0070$ | $0.2681 \pm 0.0113$ | $1111 \pm 38$ | $58.4 \pm 4.1$ | $1566 \pm 95$ | $0.0373 \pm 0.0033$ |
| H21 | $0.5773 \pm 0.0028$ | $120.37 \pm 0.42$ | $0.1701 \pm 0.0067$ | $0.2890 \pm 0.0103$ | $1153 \pm 37$ | $68.3 \pm 4.0$ | $1530 \pm 107$ | $0.0446 \pm 0.0045$ |
| H22 | $0.5929 \pm 0.0022$ | $118.93 \pm 0.36$ | $0.1593 \pm 0.0052$ | $0.2633 \pm 0.0089$ | $1202 \pm 34$ | $57.2 \pm 3.2$ | $1417 \pm 80$ | $0.0404 \pm 0.0033$ |
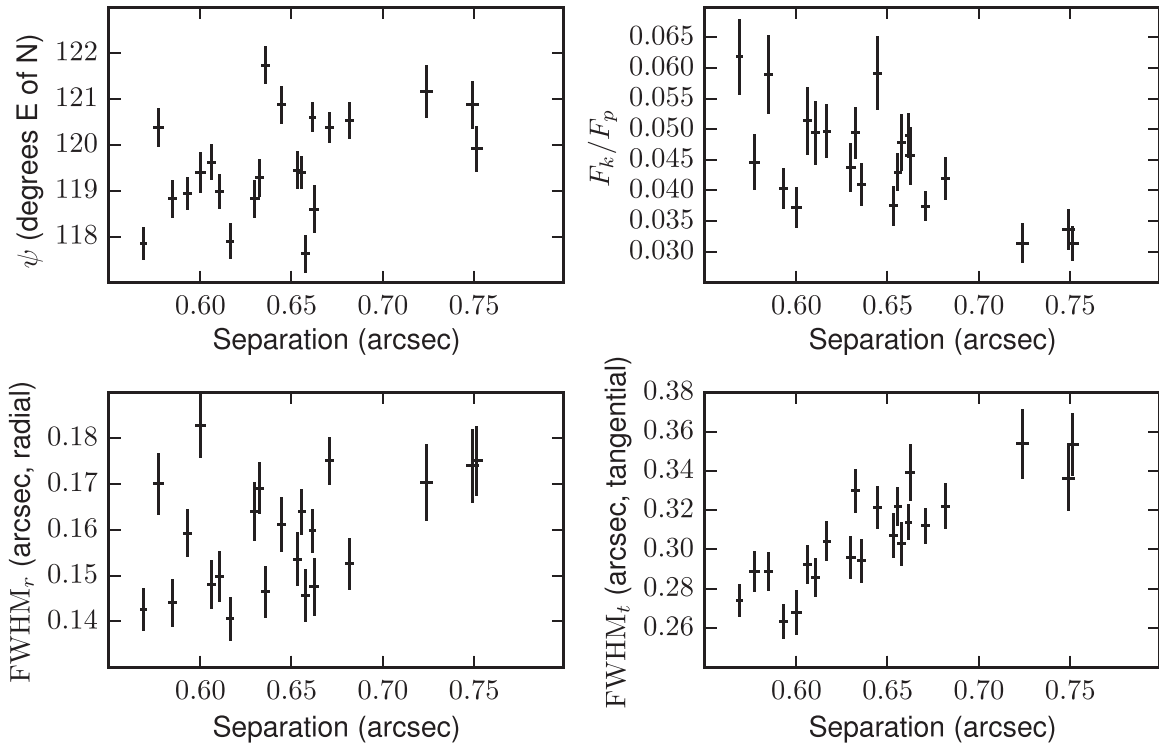


**Figure 5.** Variation of the *HST*-SVD-measured properties with separation of the inner knot from the pulsar.

knot separation. Indeed, a plot of $\gamma$-ray flux measurements that is coincident with the 22 *HST* and 12 Keck observations against the measured pulsar–knot separations (Figure 9) shows no significant correlation. The absence of a simple correlation, the relative sparsity of the near-IR and optical data, and the lack of a detailed physical model make it difficult to relate $\gamma$-ray flaring to changes in the pulsar–knot separation. Hence, while this

behavior is intriguing, we have not succeeded in deducing a pattern relating the $\gamma$-ray flares to the pulsar–knot separation. Of course, it is also possible that no such relationship exists.

We note that Moran et al. (2013) used polarization observations from the *HST* archive to measure a possible change in the linear polarization of the inner knot that occurred a few weeks after an incursion of the inner knot in 2005

**Table 7**
Results of Regression Analyses for the 22 *HST* Observations Based on the Data in Table 6

| Power-law for $r_1 = 0\farcs6421$ | | | | |
| --- | --- | --- | --- | --- |
| Property | Unit | $p(r_1)$ | Power-law Index $q$ | Probability |
| $FWHM_r$ | $''$ | $0.1584 \pm 0.0025$ | $0.41 \pm 0.21$ | 5.9E-2 |
| $FWHM_t$ | $''$ | $0.3067 \pm 0.0029$ | $0.92 \pm 0.12$ | 2.9E-7 |
| $S_k$ | $F_p/('')^2$ | $0.796 \pm 0.029$ | $-2.77 \pm 0.47$ | 9.8E-6 |
| $F_k$ | $F_p$ | $0.0440 \pm 0.0014$ | $-1.70 \pm 0.40$ | 4.1E-4 |
| Linear for $\langle r_0 \rangle = 0\farcs6440$ | | | | |
| Property | | $\psi_0(\langle r_0 \rangle)$ | $d\psi_0/dr_0$ | |
| $\psi_0$ | $°, °/''$ | $119.60 \pm 0.22$ | $10.2 \pm 4.4$ | 3.2E-2 |

**Table 8**
Results of the *Chandra* Analysis

| ObsID | Pulse Average | | | Pulse Minimum | | | $F_k/F_p$ |
| --- | --- | --- | --- | --- | --- | --- | --- |
| | Pulsar | Knot | Background | Pulsar | Knot | Background | $3\sigma$ |
| 09765 | 51844 | 2963 | 3704 | 845 | 57 | 72 | <0.0022 |
| 11245 | 5630 | 1018 | 851 | 88 | 16 | 12 | <0.0094 |
| Last 6 | 13549 | 2622 | 2503 | 203 | 39 | 44 | <0.0067 |
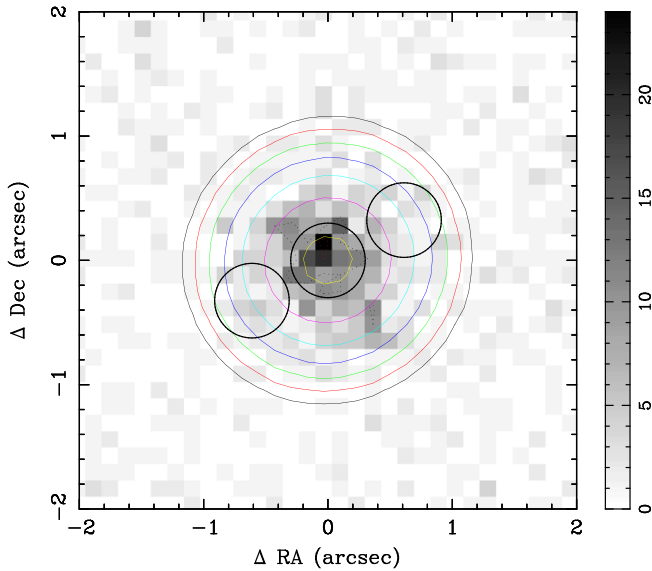


**Figure 6.** *Chandra* image at pulse minimum from the sum of the last six flaring data sets in Table 3. The three small black circles show $0\farcs3$-radius extraction regions, the central of which is used to estimate the pulsar flux. The circle, at a position angle $\psi = 120°$ east of north and $0\farcs65$ from the pulsar, is roughly centered on the average optical location of the knot. Data in the opposite small circle (the one to the NW where N is up) are used to estimate background. Large circles show the best-fit Gaussian to the phase-average pulsar data at intensity levels of 10, 20, 40, 80, 160, 320, and 640 cts/pixel illustrating the level of impact of the PSF at the site of the knot—i.e., slight but non-negligible. The intensity level is shown by the grayscale bar on the right.
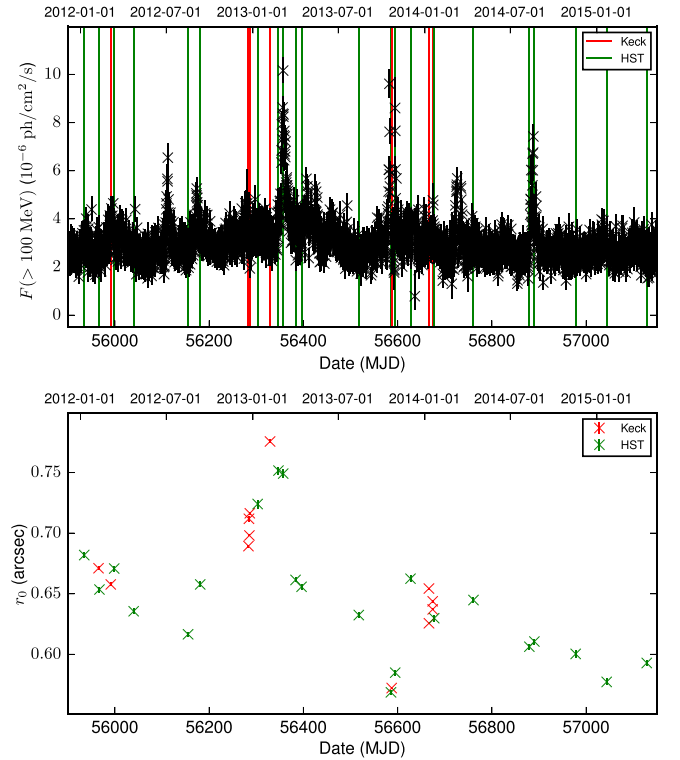


**Figure 7.** *Fermi*/LAT 12 hr average flux (upper panel) and pulsar–knot separation (lower panel) vs. time, for Keck (red) and *HST* (green) observations.

November, with an amplitude and timescale comparable to those of the 2013 October incursion that we observed. Like the 2013 October incursion, the 2005 November incursion coincided with an increase in the inner knot's optical flux. While the significance of the polarization change was marginal based upon the authors' conservative statistical analysis, we conclude that optical polarization measurements may be useful for seeking a relationship between $\gamma$-ray flaring and inner knot behavior.

## 6. IMPLICATIONS FOR THEORETICAL MODELS

In the basic model of the Crab Nebula (e.g., Rees & Gunn 1974), the pulsar wind passes through a shock at a radius $\sim 3 \times 10^{17}$ cm where the wind momentum flux balances the nebular pressure. However, the wind should be anisotropic. For example, the momentum flux in a split-monopole $\propto \sin^2 \theta$ (Bogovalov 1999) and recent simulations suggest $\propto \sin^4 \theta$ (Tchekhovskoy et al. 2013, 2015) where $\theta$ is the polar angle.

**Table 9**
*Fermi*/LAT 12 hr-average Fluxes and Pulsar–Knot Separations as Measured with Keck and *HST* (SVD Analysis)

| # | Date | $t_{mid}$ MJD | $r_0$ " | *Fermi*/LAT $\geqslant$100 MeV $10^{-6}$ ph s$^{-1}$ cm$^{-2}$ |
|---|---|---|---|---|
| H1 | 2012 Jan 08 | 55934.797 | $0.6819 \pm 0.0023$ | 2.74 (+0.42, −0.39) |
| K1 | 2012 Feb 08 | 55965.280 | $0.6711 \pm 0.0015$ | 2.64 (+0.44, −0.40) |
| H2 | 2012 Feb 10 | 55967.171 | $0.6535 \pm 0.0024$ | 2.02 (+0.43, −0.39) |
| K2 | 2012 Mar 05 | 55991.311 | $0.6577 \pm 0.0015$ | 2.70 (+0.38, −0.36) |
| H3 | 2012 Mar 12 | 55998.414 | $0.6708 \pm 0.0022$ | 3.70 (+0.43, −0.40) |
| H4 | 2012 Apr 22 | 56039.850 | $0.6356 \pm 0.0024$ | 2.40 (+0.50, −0.46) |
| H5 | 2012 Aug 16 | 56155.336 | $0.6166 \pm 0.0020$ | 2.87 (+0.44, −0.44) |
| H6 | 2012 Sep 10 | 56180.960 | $0.6577 \pm 0.0024$ | 3.06 (+0.37, −0.37) |
| K3 | 2012 Dec 22 | 56283.381 | $0.6893 \pm 0.0011$ | 2.64 (+0.45, −0.45) |
| K4 | 2012 Dec 23 | 56284.403 | $0.7118 \pm 0.0021$ | 4.56 (+0.53, −0.50) |
| K5 | 2012 Dec 24 | 56285.379 | $0.6981 \pm 0.0007$ | 3.59 (+0.50, −0.45) |
| K6 | 2012 Dec 25 | 56286.370 | $0.7164 \pm 0.0010$ | 1.89 (+0.43, −0.39) |
| H7 | 2013 Jan 10 | 56302.992 | $0.7240 \pm 0.0035$ | 2.68 (+0.51, −0.51) |
| K7 | 2013 Feb 06 | 56329.248 | $0.7756 \pm 0.0013$ | 3.17 (+0.50, −0.50) |
| H8 | 2013 Feb 24 | 56347.055 | $0.7516 \pm 0.0031$ | 4.29 (+0.55, −0.51) |
| H9 | 2013 Mar 06 | 56357.023 | $0.7491 \pm 0.0033$ | 10.88 (+0.47, −0.47) |
| H10 | 2013 Apr 01 | 56383.320 | $0.6614 \pm 0.0019$ | 4.05 (+0.50, −0.50) |
| H11 | 2013 Apr 14 | 56396.113 | $0.6557 \pm 0.0021$ | 3.43 (+0.50, −0.50) |
| H12 | 2013 Aug 13 | 56517.710 | $0.6324 \pm 0.0023$ | 2.56 (+0.38, −0.35) |
| H13 | 2013 Oct 20 | 56585.793 | $0.5687 \pm 0.0019$ | 3.83 (+0.23, −0.23) |
| K8 | 2013 Oct 22 | 56587.443 | $0.5722 \pm 0.0004$ | 0.70 (+1.41, −0.51) |
| H14 | 2013 Oct 29 | 56594.700 | $0.5849 \pm 0.0022$ | 7.08 (+0.79, −0.79) |
| H15 | 2013 Dec 01 | 56627.273 | $0.6624 \pm 0.0026$ | 2.76 (+0.47, −0.45) |
| K9 | 2014 Jan 09 | 56666.316 | $0.6543 \pm 0.0006$ | 3.14 (+0.40, −0.40) |
| K10 | 2014 Jan 09 | 56666.438 | $0.6257 \pm 0.0003$ | 3.13 (+0.39, −0.37) |
| K11 | 2014 Jan 17 | 56674.356 | $0.6371 \pm 0.0008$ | 4.29 (+0.46, −0.45) |
| K12 | 2014 Jan 17 | 56674.400 | $0.6438 \pm 0.0009$ | 3.93 (+0.39, −0.37) |
| H16 | 2014 Jan 20 | 56677.530 | $0.6299 \pm 0.0026$ | 3.37 (+0.37, −0.37) |
| H17 | 2014 Apr 13 | 56760.900 | $0.6448 \pm 0.0024$ | 3.84 (+0.52, −0.52) |
| H18 | 2014 Aug 10 | 56879.375 | $0.6063 \pm 0.0022$ | 2.50 (+0.41, −0.41) |
| H19 | 2014 Aug 21 | 56890.094 | $0.6106 \pm 0.0023$ | 3.56 (+0.26, −0.25) |
| H20 | 2014 Nov 16 | 56977.820 | $0.6004 \pm 0.0029$ | 2.50 (+0.43, −0.39) |
| H21 | 2015 Jan 21 | 57043.620 | $0.5773 \pm 0.0028$ | 3.05 (+0.36, −0.34) |
| H22 | 2015 Apr 16 | 57128.670 | $0.5929 \pm 0.0022$ | 2.62 (+0.43, −0.43) |

As a result, the shock is likely to be quite oblate. The sections of the shock near the poles would be oblique and much closer to the pulsar than the equatorial part. The observed radiation presumably comes from relativistic particles (electrons or positrons) accelerated behind the shock. Since the outflow from an oblique shock can remain relativistic, we would be able to see a compact, emitting feature (the inner knot) if the relativistic outflow happens to be aligned with our line of sight so that its emission is beamed. The inner knot should appear to us as having some offset from the pulsar due to the deflection of the outflow from its presumed radial motion (Figure 10). If the shock is approximately axisymmetric as one would expect, the projected emitting site would fall on the projected symmetry axis, leading to an alignment with the jet. The shape of the inner knot should also be more or less symmetric about the axis; whether it is elongated parallel or perpendicular to the axis depends on the geometry of the oblique shock. Furthermore, the synchrotron emission should be linearly polarized (Komissarov & Lyutikov 2011; Y. Yuan & R. Blandford 2015, in preparation).

The shock model predicts that the scaling between the observed properties of the knot—projected pulsar–knot separation $r_0$, tangential angular width FWHM$_t$, radial angular width FWHM$_r$, and surface brightness $S_k$—should be determined by the upstream magnetization $\sigma \equiv B_1^2 / \mu_0 n_1 \gamma_1^2 mc^2$ (where $m$ is

electron mass and $B_1$, $n_1$, $\gamma_1$ are upstream magnetic field, proper density, bulk Lorentz factor, respectively) plus three more parameters that characterize the shape of the shock near the emitting site: the unprojected pulsar–knot separation $r_k$; the incident angle $\delta_1$, defined to be the angle between upstream velocity and the shock surface as shown in Figure 10; and the shock poloidal radius of curvature $R_c$.

Let the outflow be deflected from the radial direction by an angle $\Delta$ at the shock. We then have $r_0 = r_k \Delta$. The knot tangential size is determined by the Doppler beaming and the shock radius of curvature in the toroidal direction as FWHM$_t \approx 2r_k/\gamma$, where $\gamma$ is the downstream Lorentz factor. In the simplest shock model with an isotropic plasma, both $\Delta$ and $\gamma$ are functions of $\sigma$ and $\delta_1$: $\Delta = \delta_1 - \arctan(\chi \tan \delta_1)$ and $\gamma = 1/(\sin \delta_1 \sqrt{1 - \chi^2})$, where $\chi \equiv v_{2\perp}/v_{1\perp} = B_1/B_2 = (1 + 2\sigma + \sqrt{16\sigma^2 + 16\sigma + 1})/6(1 + \sigma)$ is the compression ratio at the shock, $v_{1,2\perp}$ being the component of upstream/ downstream velocity perpendicular to the shock (Komissarov & Lyutikov 2011). The radial knot size FWHM$_r$ should also be proportional to $r_k/\gamma$ but will have an additional factor involving the ratio $R_c/r_k$.

As to the intensity, we assume that the emitting particles have a power-law distribution $\propto n' \gamma'^{-p}$ in the fluid rest frame, where $n'$ and $\gamma'$ are particle density and Lorentz factor in the
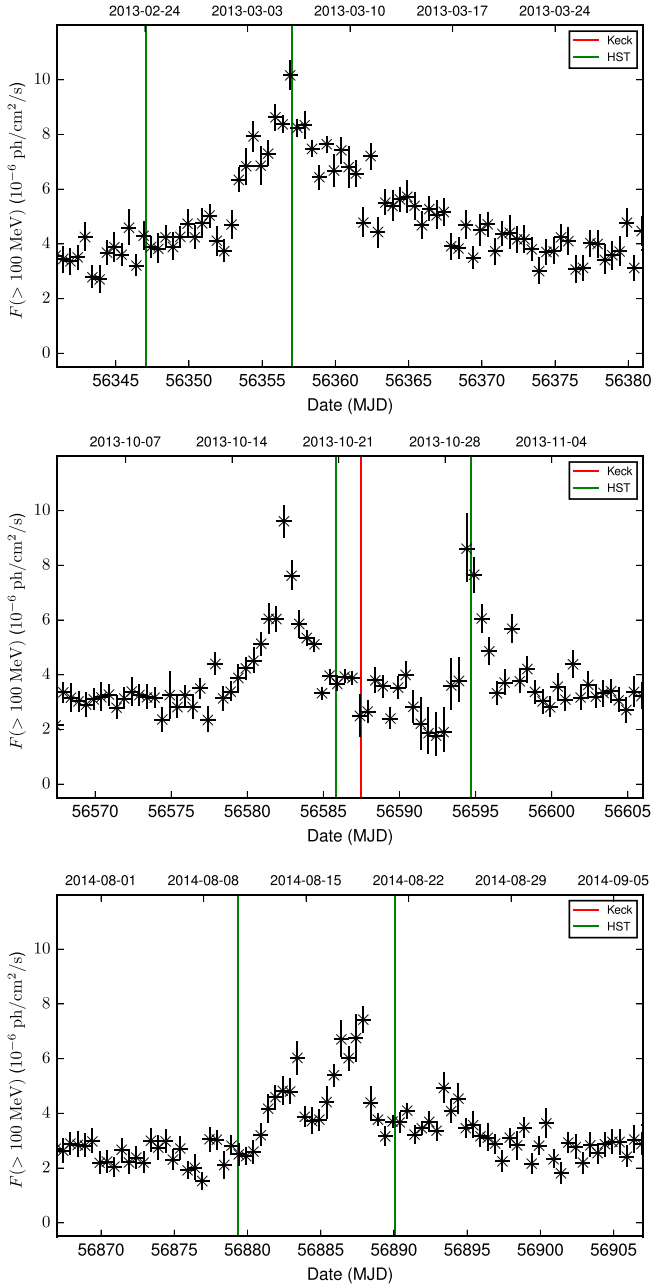
**Figure 8.** *Fermi*/LAT 12 hr average fluxes during Keck (red) and *HST* (green) observations at the time of the largest $\gamma$-ray flares in 2013 March (top), in 2013 October (middle), and in 2014 August (bottom).
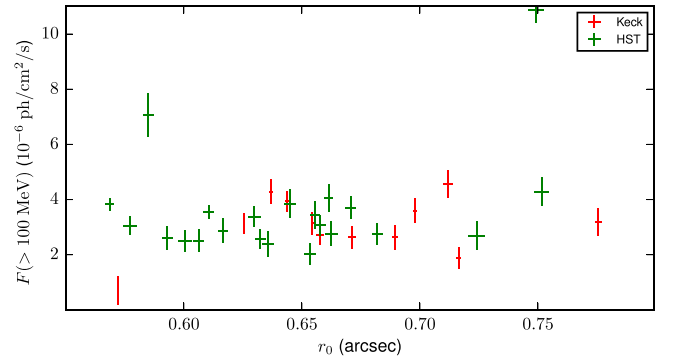


**Figure 9.** *Fermi*/LAT 12-hr-average fluxes centered on the times of Keck (red) and *HST* (green) measurements of pulsar–knot separations.

one takes the maximum Doppler factor $\mathcal{D} \approx 2\gamma$, and we get $S_{\nu,\text{peak}} \propto nB^{(p+1)/2}\ell$ where $\ell$ is an estimation of the length of the emitting region along the line of sight. As roughly $B \propto r_k^{-1}$ and $n \propto r_k^{-2}$, we have $S_{\nu,\text{peak}} \propto r_k^{-2-(p+1)/2}\ell$.

These previous relations allow us to set the constraints discussed below using both the steady and variable properties of the knot.

### 6.1. Variability

In the shock model, variability can arise either upstream or downstream of the shock. First, stress tensor variation in the nebula can cause the shock radius and shape to vary over time. Three-dimensional MHD simulations (Porth et al. 2014) show that even if the upstream condition is fixed, the post-shock flow can be quite variable: there is vortex-shedding from the termination shock, and the shock constantly interacts with waves and vortices in the nebula. Those variations are expected to be mostly magnetic in origin, and the interactions between the shock and the downstream flow are quite nonlinear. The picture is similar to earlier 2D simulations (e.g., Camus et al. 2009) except that the kink instability sets in so that the hoop compression is less prominent as in the 2D case; also short-term variability is less pronounced. The 3D simulations give a typical variation timescale of less than one year.

Now suppose that the change of downstream pressure causes the shock radius $r_k$ to change. For simplicity we first assume that $\Delta$, $\ell$, $\gamma$, and $p$ stay more or less the same, then from the above scaling relations, we have $S_{\nu,\text{peak}} \propto r_0^{-2-(p+1)/2}$, $\text{FWHM}_t \propto r_0$, and knot flux $F_\nu \propto S_{\nu,\text{peak}}\text{FWHM}_t\text{FWHM}_r \propto r_0^{-(p+1)/2}$, assuming $\text{FWHM}_r$ to also be roughly proportional to $r_k$. In reality $\Delta$, $\ell$, and $\gamma$ change with the shock radius $r_k$ as well, as the shock shape and upstream incident angle $\delta_1$ vary. Consequently, the observed correlation is more complicated and less clean; however, the general trend is consistent with our expectation of the shock model. In the 3D simulation of Porth et al. (2014), the synthetic images of the knot show a variation consistent with the observations of Moran et al. (2013), suggesting that downstream variation of the shock could provide a good explanation for the knot variability.

Variations initiated by the pulsar can also cause the knot properties to change. In such a scenario, the shortest possible variation timescale is $t_\nu \sim r_k(1-\cos(1/\gamma))/c \sim r_k/(2\gamma^2 c) \sim 1\,\text{day}(r_k/10^{17}\,\text{cm})(\gamma/5)^{-2}$ up to 10% inaccuracy assuming $\gamma \gtrsim 3$. However, there is no evidence in the pulsar timing that this is actually happening.
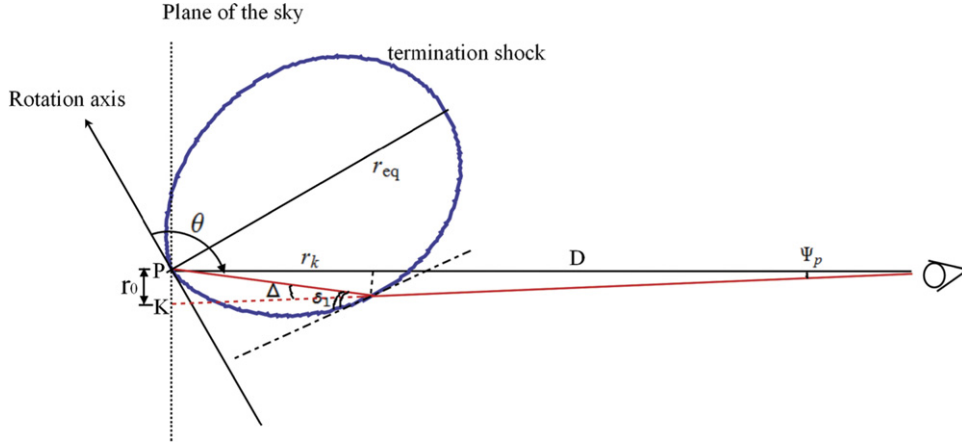
same reference frame, and $p \sim 2.6$ from the measured spectral index of the knot (Sollerman 2003; Melatos et al. 2005).

The emissivity in the fluid rest frame is $j'_\nu(\nu') \propto n'B'^{(p+1)/2}\nu'^{-(p-1)/2}$, where $B'$ and $\nu'$ are the magnetic field and the radiation frequency measured in this reference frame. After transforming to the nebula frame, the emissivity has a dependence on the flow Lorentz factor $\gamma$, particle (improper) number density $n$, and magnetic field $B$ as follows: $j_\nu \propto \mathcal{D}^{2+(p-1)/2}(n/\gamma)(B/\gamma)^{(p+1)/2}$, where $\mathcal{D} = \nu/\nu' = \sqrt{1-\beta^2}/(1-\boldsymbol{\beta}\cdot\boldsymbol{n})$ is the Doppler factor, in which $\boldsymbol{\beta}$ is the flow velocity and $\boldsymbol{n}$ is a unit vector along the direction of the line of sight. The surface brightness corresponds to the emissivity integrated along the line of sight in the nebular frame: $S_\nu = \int j_\nu\,dl$. To estimate the peak surface brightness,

**Figure 10.** Geometry of the termination shock on the meridional plane determined by the pulsar rotation axis and the observer's line of sight toward the pulsar (point P). The angle between the line of sight and the pulsar rotation axis is $\theta_{ob} = 2\pi/3$, consistent with that measured by Ng & Romani ([2008]). The inner knot (point K) is projected on the plane of the sky at an angle of $\Psi_p = r_0/D \approx 0\rlap{.}''65$ southeast of the pulsar. (NB: Throughout this paper, $r_0$ appears in units of arcseconds.) The angle between the upstream velocity and the shock surface is $\delta_1$; the outflow is deflected from the radial direction by an angle $\Delta$.

### 6.2. Time-averaged Properties of the Knot

The properties of the knot may be used to set constraints on the flow composition and how much dissipation occurs at the shock. One constraint comes from geometrical relations among the three measured angles $r_0$, $\mathrm{FWHM}_t$, and $\mathrm{FWHM}_r$. For the simplest shock model, we have $r_0 = r_k \Delta$ and $\mathrm{FWHM}_t \approx r_k/\gamma$, where $\Delta$ and $\gamma$ only depend on $\sigma$ and $\delta_1$, such that the ratio $\mathrm{FWHM}_t/r_0$ sets limit on $\sigma$ and $\delta_1$. We find that $\mathrm{FWHM}_t/r_0 = 2/(\gamma\Delta) = 2\sin\delta_1\sqrt{1-\chi^2}/[\delta_1 - \arctan(\chi\tan\delta_1)] \geqslant 2.8$, with the minimum at $\sigma = 0$ and $\delta_1 = 0.39$. In contrast, the observation gives $\mathrm{FWHM}_t \sim 0.5r_0$, indicating that some important ingredient is missing in the standard shock model. For example, the upstream flow might have already been bent before arriving at the shock; and/or the anisotropic particle distribution downstream might be important in determining the size of the knot. Although more detailed investigations will be described elsewhere, the above discussion on variability and the following discussion on energetics should be valid for quite general shock models.

The shape of the knot also has some interesting implications. In both the *Hubble* and Keck images, the knot is not just a simple ellipse that only involves quadratic terms of coordinates; it has curvature and appears to be convex away from the pulsar ("smile"), so at least a third moment of the coordinates is needed to describe the shape. A simple intuitive picture is based on the geometry that the shock surface is similar to a torus centered on the pulsar and we look through the hole from the bottom. If emission from the shock outflow roughly follows the local toroidal magnetic field, one would imagine the knot to be convex toward the pulsar ("frown")—contradictory to what we see. In fact, we should not overlook the possibility that the outflow may have significant bending downstream. If the outflow bends toward the equator by an angle $\sim 1/\gamma$ within the emission length, we would see the knot more extended (contracted) on the far (near) side with respect to the pulsar, as additional flow lines enter (originally aligned flow lines leave) the emission cone on the corresponding side.

Another constraint comes from the observed flux of the knot. In the $K'$ band, the typical knot–pulsar flux ratio is $\sim 0.063$ (Table [4]). If we take the photometry of the pulsar from Sandberg & Sollerman ([2009]), the pulsar $K_s$ band magnitude is $13.80 \pm$

0.01, after dereddening with the best-fit value $E(B-V) = 0.52$ (Sollerman et al. [2000]) and the extinction law from Fitzpatrick ([1999]), this corresponds to a flux of $2.2 \times 10^{-26}$ erg s$^{-1}$ cm$^{-2}$Hz$^{-1}$. So the inner knot flux in $K'$ band should be roughly $F_\nu^{\mathrm{knot}} = 1.4 \times 10^{-27}$ erg s$^{-1}$ cm$^{-2}$ Hz$^{-1}$. Similarly, optical data (Table [6]) on average give a dereddened flux of $F_\nu^{\mathrm{knot}} = 1 \times 10^{-27}$ erg s$^{-1}$ cm$^{-2}$ Hz$^{-1}$. However, we do not attempt here to get a spectral index using the time-averaged fluxes due to the variability of the knot and the fact that most of the multi-wavelength observations are not simultaneous. Previous measurements by Sollerman ([2003]) and Melatos et al. ([2005]) indicate that the spectrum of the knot in IR to optical range is a power law $F_\nu \propto \nu^{-\alpha}$ with $\alpha \sim 0.8$, and Melatos et al. ([2005]) further measured that this power law extends to NUV (160–320 nm), with a flux in NUV $F_\nu^{\mathrm{knot}} = 0.12$ mJy $= 1.2 \times 10^{-27}$ erg s$^{-1}$ cm$^{-2}$ Hz$^{-1}$—this is the highest energy at which the knot has been measured. A few more recent measurements show slightly different spectral index ranging from 0.63 (Tziamtzis et al. [2009]) to 1.3 (Sandberg & Sollerman [2009]), but unfortunately these are based on non-simultaneous data. It would be very interesting to refine the spectral measurement using near simultaneous IR/optical images in the future. In what follows we adopt a fiducial spectral model $F_\nu^{\mathrm{knot}} \sim 10^{-27}(\nu/10^{15}\,\mathrm{Hz})^{-0.8}$ erg s$^{-1}$ cm$^{-2}$ Hz$^{-1}$ with the caveat that this could change with better observations.

Using the above spectral model, we find that the knot integrated flux in the IR/optical band ($(0.1-2) \times 10^{15}$ Hz) is $F_{\mathrm{O/IR}}^{\mathrm{knot}} = 2.6 \times 10^{-12}$ erg s$^{-1}$cm$^{-2}$. Thus, the luminosity of the knot per steradian is $L_{\mathrm{O/IR},\Omega} = D^2 F_{\mathrm{O/IR}}^{\mathrm{knot}} = 10^{32}$ erg s$^{-1}$, where $D \sim 2$ kpc is the distance of the Crab. If we define $\epsilon \equiv L_{\mathrm{O/IR},\Omega}/(\dot{E}/4\pi)$, where $\dot{E} = 5 \times 10^{38}$ erg s$^{-1}$ is the pulsar spin-down power, $\epsilon$ can be used as a measure of the radiative efficiency of the shock along the direction of line of sight in IR to optical range. Here we find $\epsilon = 2.5 \times 10^{-6}$ and the shock is highly adiabatic.

We can obtain an estimation of the enthalpy fraction of IR/optical-emitting particles in the downstream flow

$$\eta(\gamma') = \frac{8}{3} \frac{\gamma t_{\mathrm{cool}}'}{t_{\mathrm{flow}}} \frac{\nu L_{\nu,\Omega}}{\dot{E}/(4\pi)} = \frac{8}{3} \frac{\gamma t_{\mathrm{cool}}'}{t_{\mathrm{flow}}} \frac{\nu L_{\nu,\Omega}}{\dot{E}/(4\pi)}, \qquad (1)$$

where $t_{\mathrm{flow}}$ is the flow timescale and $t'_{\mathrm{cool}} = 6\pi\epsilon_0 m^3 c^3/(e^4 B'^2 \gamma') \approx 10^2 \gamma^2 B_{-3}^{-3/2} \nu_{14}^{-1/2}$ years is the synchrotron cooling time of the particles in the fluid rest frame (we have adopted $B = B_{-3}$ mG and $\nu = \nu_{14} 10^{14}$ Hz for the numerical value). Thus the particle injection rate per unit steradian in the corresponding energy band is

$$\dot{N}\left(\gamma'\right) = \frac{3\eta\left(\gamma'\right)}{4\gamma' mc^2} \frac{\dot{E}}{4\pi\gamma}. \qquad (2)$$

Adopting typical values $\gamma = 5\gamma_5$, $t_{\mathrm{flow}} = r_{17} 10^{17}$ cm/$c$, we find that for IR-emitting particles, $\eta_{\mathrm{IR}} = 0.05\gamma_5^3 B_{-3}^{-3/2} r_{17}^{-1}$, and $\dot{N}_{\mathrm{IR}} = 2 \times 10^{36} \gamma_5^2 B_{-3}^{-1} r_{17}^{-1}$ s$^{-1}$ sr$^{-1}$. The spectral index of the knot indicates that the particle distribution power-law index should be $p \sim 2.6$, thus the IR-emitting particles should comprise the majority of particle pressure downstream. From the above estimations, it seems that the particle injection rate at the shock is marginally consistent with the scenario that most of the IR/optical-emitting particles are provided by the shock.

Regarding particle acceleration mechanisms, we notice that IR-emitting particles usually go through $N = t_{\mathrm{flow}}\nu_g$ Larmor orbits, where $\nu_g = \nu_B/\gamma'$ is the relativistic gyrofrequency—the cyclotron frequency ($\nu_B$) divided by the electron's Lorentz factor ($\gamma'$). Eliminating $\gamma'$ in favor of the magnetic field ($B$) and observing frequency ($\nu$), the number of orbits within the flow timescale is $N \approx 6 \times 10^4 B_{-3}^{3/2} r_{17} \nu_{14}^{-1/2}$. To allow sufficient time for acceleration mechanisms requiring instabilities or stochastic processes to operate, requires that $N \gg 1$. However, for particles emitting $\gamma$ rays of energy 300 MeV, $N \lesssim 1$, thus requiring special acceleration mechanisms—if the emitting electrons are indeed accelerated at the shock.

One more constraint comes from the polarization of the knot. Most recent polarimetry performed by Moran et al. (2013) gives a high polarization degree of ∼60%, with position angle aligned with the symmetry axis, indicating a strongly toroidal magnetic field. Here we need to be careful about the depolarization effect due to relativistic kinematics (Lyutikov et al. 2003). What happens then is that Lorentz transformation of the emission of a relativistic plasma from the comoving frame to the lab frame produces a rotation of the polarization vector. For a curved emitting surface, neighboring fluid elements have slightly different velocities, thus their polarization vectors experience different amounts of rotation. As one sums the contribution from the visible surface (this is essentially what we observe), the result is some degree of depolarization. We find that for the oblique shock in the Crab Nebula, under an ultrarelativistic approximation, the upper limit of polarization degree is similar to that in Lyutikov et al. (2003): 56.25% for particle spectral index $p = 3$ and 43.4% for $p = 2$. Thus, the observed high degree of polarization and its possible variation are highly constraining on theoretical models. Mildly relativistic outflow may give a higher polarization degree but may not produce a small enough knot (see Porth et al. 2014). In addition, particle acceleration mechanisms that generate turbulence could further depolarize the emission. It would be interesting to repeat this polarization observation, especially with AO.

## 7. CONCLUSIONS

We have (1) introduced a new approach for analyzing time series images; (2) discovered that the key properties of the knot (radial width, tangential width, flux) are correlated with the time-variable separation between the knot and the pulsar; (3) shown that with the available data it is not possible to determine a strong correlation between the knot separation and the occurrence of $\gamma$-ray flares; (4) set an upper limit to the low-energy X-ray flux from the inner knot; and (5) discussed the implications of our observations to set constraints on particular elements of the standard shock modeling of the relativistic outflow from the pulsar. These include inferences as to wind magnetization $\sigma$, shock shape parameters such as incident angle $\delta_1$, and poloidal radius of curvature $R_c$, as well as the IR/optical-emitting particle enthalpy fraction. We found that while the standard shock model gives good agreements with observations in many aspects, there remain two puzzles: (a) the angular size of the knot relative to the pulsar–knot separation is much smaller than expected; and (b) the variable yet high degree of polarization is difficult to reconcile with a highly relativistic outflow (see, however, Porth et al. 2014). We also found that the IR/optical flux of the inner knot is marginally consistent with the scenario in which the shock accelerates most of the optical-emitting particles in the nebula.

## APPENDIX
## DATA ANALYSIS

### A.1. Keck

To study the knot using the high-resolution Keck adaptive optics (AO) data, we characterize the region around the pulsar using an empirically measured PSF and an analytical model of the knot geometry.

## Pulsar & Knot

## PRF Star
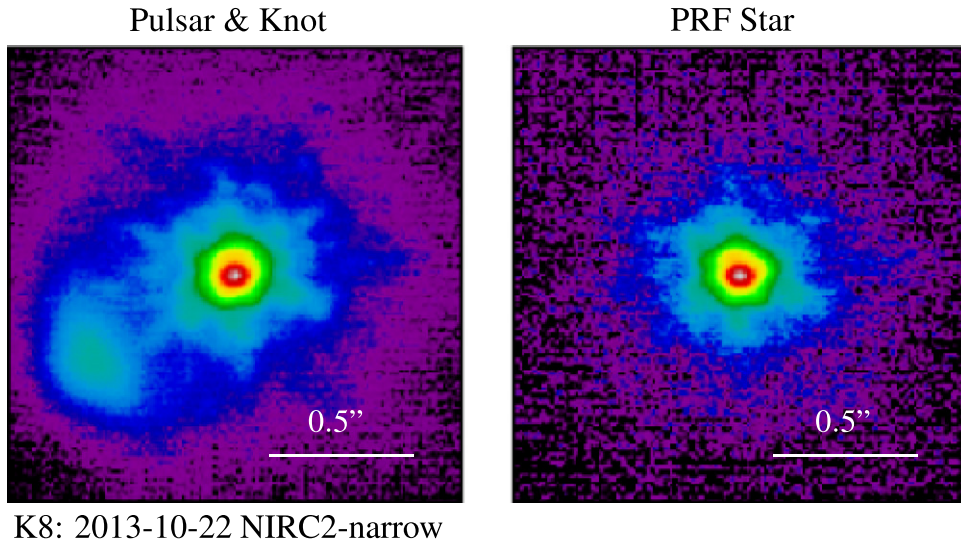


K8: 2013-10-22 NIRC2-narrow

**Figure 11.** Pulsar (left) and a nearby star (right) from Keck data taken on 2013 October 22. (a) An *H* filter image of the pulsar and knot (in the lower-left) as seen by the NIRC2-narrow camera ($0\!''01$ pixels and a $10'' \times 10''$ field of view). The structure of the knot is resolved and separated from the pulsar by a statistically significant valley. (b) A nearby ($5''$) comparison star, used to establish the point-response-function. Both images are shown with a logarithmic color stretch.

**Table 10**
Results of the Traditional Analysis of the First 17 *HST* Observations

| # | $r_0$ | FWRMS$_r$ | FWRMS$_t$ | $F_k$ |
|---|---|---|---|---|
| | $''$ | $''$ | $''$ | e/s |
| H1 | $0.660 \pm 0.012$ | $0.287 \pm 0.019$ | $0.551 \pm 0.037$ | $116.5 \pm 2.9$ |
| H2 | $0.634 \pm 0.012$ | $0.283 \pm 0.020$ | $0.538 \pm 0.038$ | $110.9 \pm 2.8$ |
| H3 | $0.649 \pm 0.013$ | $0.333 \pm 0.021$ | $0.594 \pm 0.038$ | $131.6 \pm 3.3$ |
| H4 | $0.615 \pm 0.012$ | $0.255 \pm 0.020$ | $0.489 \pm 0.038$ | $90.4 \pm 2.3$ |
| H5 | $0.588 \pm 0.012$ | $0.278 \pm 0.019$ | $0.560 \pm 0.038$ | $112.9 \pm 2.8$ |
| H6 | $0.635 \pm 0.012$ | $0.290 \pm 0.020$ | $0.552 \pm 0.037$ | $111.6 \pm 2.8$ |
| H7 | $0.706 \pm 0.010$ | $0.288 \pm 0.021$ | $0.589 \pm 0.044$ | $97.6 \pm 2.4$ |
| H8 | $0.734 \pm 0.017$ | $0.336 \pm 0.024$ | $0.658 \pm 0.046$ | $109.2 \pm 2.7$ |
| H9 | $0.732 \pm 0.013$ | $0.319 \pm 0.022$ | $0.650 \pm 0.046$ | $108.1 \pm 2.7$ |
| H10 | $0.641 \pm 0.009$ | $0.299 \pm 0.020$ | $0.580 \pm 0.039$ | $117.6 \pm 2.9$ |
| H11 | $0.637 \pm 0.011$ | $0.314 \pm 0.020$ | $0.561 \pm 0.036$ | $129.2 \pm 3.2$ |
| H12 | $0.613 \pm 0.012$ | $0.258 \pm 0.017$ | $0.578 \pm 0.039$ | $121.3 \pm 3.0$ |
| H13 | $0.547 \pm 0.009$ | $0.224 \pm 0.015$ | $0.491 \pm 0.033$ | $119.2 \pm 3.0$ |
| H14 | $0.552 \pm 0.009$ | $0.236 \pm 0.015$ | $0.511 \pm 0.033$ | $124.8 \pm 3.1$ |
| H15 | $0.631 \pm 0.012$ | $0.268 \pm 0.018$ | $0.588 \pm 0.040$ | $115.2 \pm 2.9$ |
| H16 | $0.614 \pm 0.011$ | $0.266 \pm 0.025$ | $0.519 \pm 0.049$ | $116.9 \pm 2.9$ |
| H17 | $0.624 \pm 0.012$ | $0.259 \pm 0.024$ | $0.549 \pm 0.050$ | $127.8 \pm 3.2$ |

**Table 11**
Results of Regression Analyses for the First 17 *HST* Observations Based on the Traditional Data Analysis

| Power-law for $r_1 = 0\!''6342$ | | | Power-law | |
|---|---|---|---|---|
| Property | Unit | $p(r_1)$ | Index $q$ | Probability |
| FWRMS$_r$ | $''$ | $0.2801 \pm 0.0046$ | $1.14 \pm 0.21$ | 6.0E-5 |
| FWRMS$_t$ | $''$ | $0.5605 \pm 0.0067$ | $0.85 \pm 0.15$ | 4.9E-5 |
| $F_k$ | e/s | $114.8 \pm 2.6$ | $-0.39 \pm 0.29$ | 1.9E-1 |

deconvolution of the shape of the knot made insignificant differences to the fit values and uncertainty.

### A.1.3. Knot Model

To fit the geometric parameters of the knot, we masked out the center diffraction-limited core of the pulsar, and used a Levenburg–Marquadt fitting technique to fit a two-dimensional Gaussian to the shape of the Knot.

We used a model of the form $S(r, \psi) = S_b + S_k \exp\left(-\frac{1}{2}\left((r - r_0)^2/\sigma_r^2 + (\psi - \psi_0)^2/\sigma_\psi^2\right)\right)$.

We also allowed the center of the coordinate system $(x_0, y_0)$ to vary slightly ($0\!''05$). To determine the fit uncertainties, we used the $1\sigma$ errors from the self-covariance of the fit parameters. Results were tabulated in Table 4.

### A.2. HST

#### A.2.1. HST—Traditional Analysis

In order to measure the knot properties (position, flux, tangential, and radial width) we used the SExtractor package (Bertin & Arnouts 1996). SExtractor has been extensively used for the analysis of *HST* data, in particular for the ACS camera (e.g., for the *Hubble* Ultra Deep Field project, Beckwith et al. 2006). For source detection, we require a minimum of five contiguous pixels with a detection threshold $5\sigma$ above the rms background, with a total of 32 deblending subthresholds, and
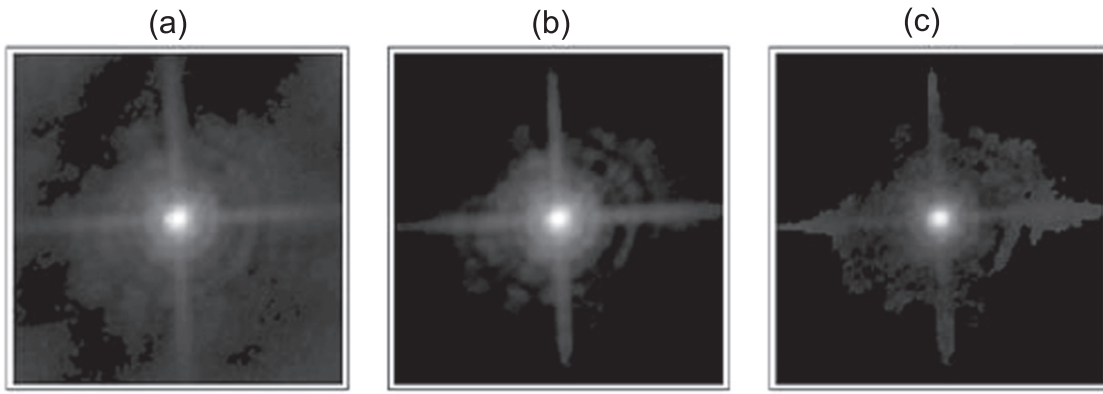
### A.1.1. PSF Subtraction

We subtracted the PSF of the pulsar using a nearby PSF star (Figure 11). During our observations, the laser guide star, and thus the center of the anisoplanatic patch, was aimed at the point halfway between the PSF star and the pulsar. We fit the PSF star, a background plus a power-law based seeing-disk, to the pulsar. For the fit, we excluded the region in the pulsar sub-image that surrounds the knot and used the other $270°$. The background was fit with a sloping plane model to allow for the variable nebular background in the pulsar and PSF star sub-images. The fitting was performed with a Levenburg–Marquadt fitter.

### A.1.2. Deconvolution

We chose not to deconvolve the knot with the empirically measured PSF. Tests on several images showed that

(a)                                          (b)                                          (c)



**Figure 12.** Images illustrating the steps in determining the *HST*/ACS PSF for this analysis: (a) extract 418 (19 × 22) 121 × 121 pixel (6″05 × 6″05) images and subtract a linear-gradient background for 19 isolated stars in these 22 *HST*/ACS observations of the Crab; (b) register images of stars and use singular-value decomposition (SVD) to determine a basis describing the PSF (first SVD component shown); and (c) model the pulsar image using the first 72 SVD components.
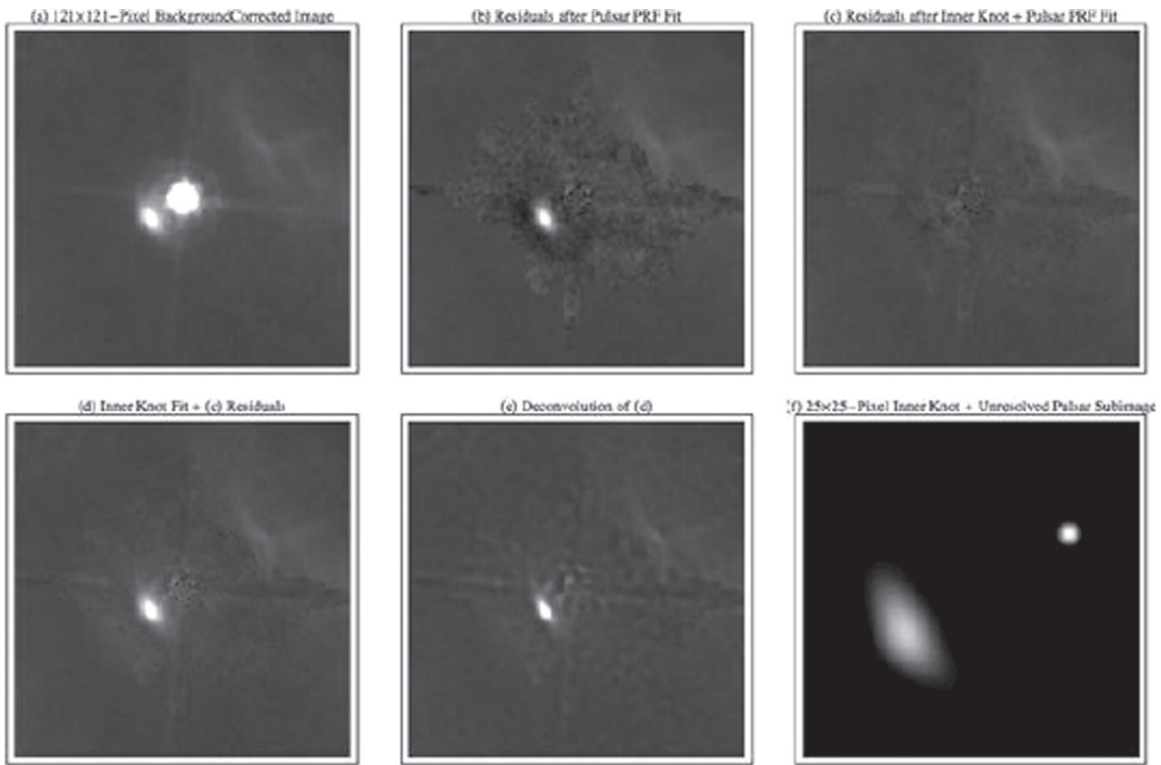


**Figure 13.** Images further illustrating steps in processing *HST*/ACS images of the Crab pulsar and inner knot: (a) subtract a linear-gradient background in the central 121 × 121 pixel (6″05 × 6″05) image of the pulsar and inner knot; (b) remove the pulsar using SVD model of PSF leaving inner knot; (c) remove the inner knot using its SVD model leaving residual background; (d) add the SVD model of the inner knot to the residual background; (e) apply the Richardson–Lucy algorithm to generate a deconvolved image of the inner knot (and residual background); and (f) synthesize the 25 × 25 pixel (1″25 × 1″25) sub-image of the registered (unresolved) pulsar and SVD model of the inner knot.

with a contrast parameter of 0.005, setting the background mesh size to 16 × 16 ACS pixels.

The position of a source is evaluated by SExtractor as the barycenter of the source brightness distribution. Flux is computed within an elliptical aperture, using an implementation of the method by Kron (1980). Note that the pulsar is not saturated and that diffraction spikes from the pulsar that might cross the inner knot only marginally affect its flux measurements. The parameters of this ellipse (semiaxes and orientation), evaluated using the second moments of the object's brightness distribution also yield a measure of the object morphology. Indeed, for the case of the knot, the direction of

the minor axis of the ellipse turned out to be consistent with the pulsar–knot direction in all images. Thus, the minor axis and the major axis of the ellipse measure the rms full widths (FWRMS) in the radial and tangential directions, respectively.

In order to assess systematic errors, we performed simulations with the ESO/MIDAS software.[13] We added to the ACS images a "synthetic knot." To generate such an artificial source, we assumed a two-dimensional Gaussian brightness distribution, with the minor axis aligned with the true pulsar–knot direction. The synthetic knot was positioned to the NW of the
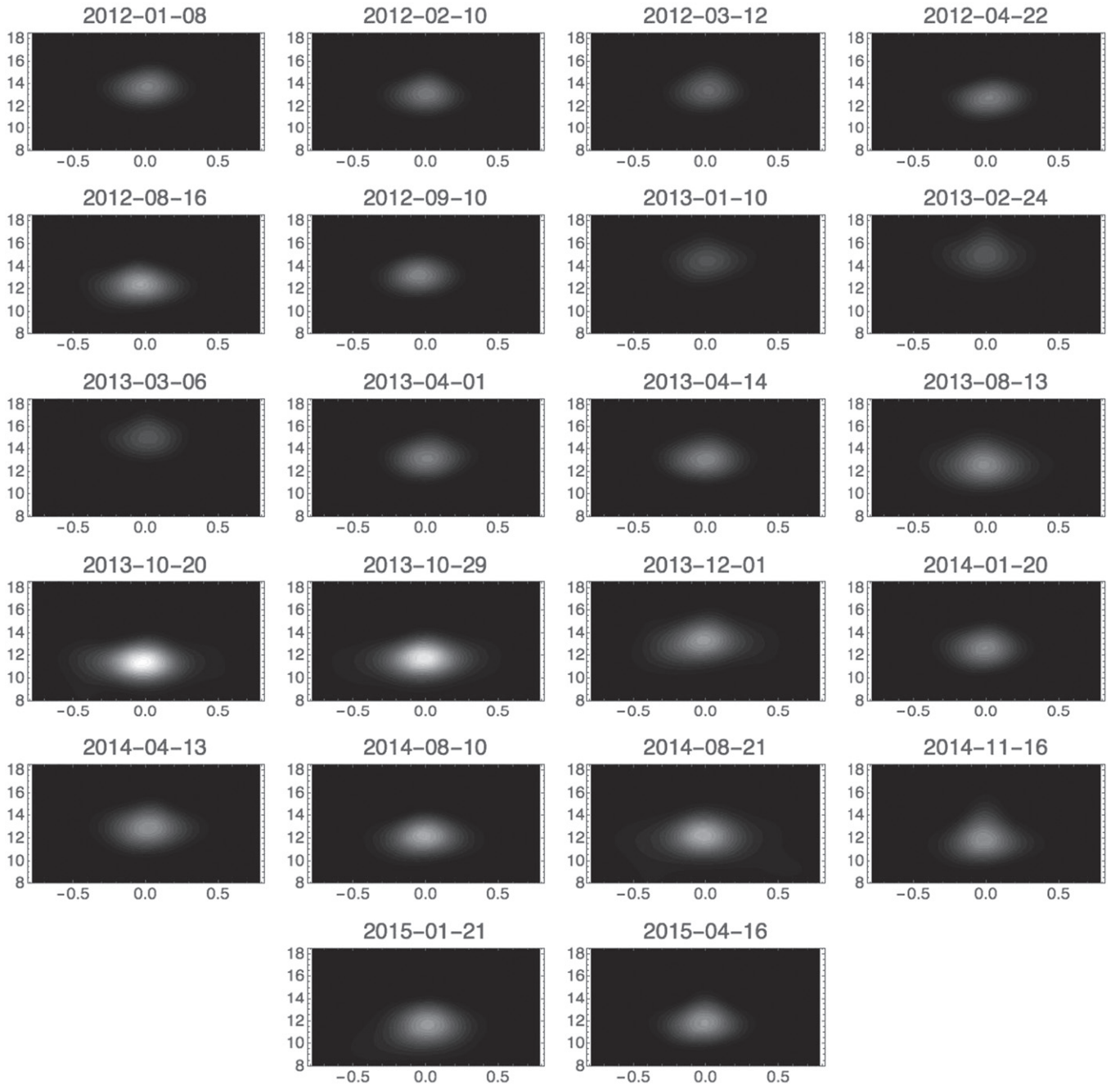
_____
[13] https://www.eso.org/sci/software/esomidas/

**Figure 14.** Mapping of processed images of the inner knot onto a $\psi$–$r$ grid. Here $\psi$ is the angular displacement in radians from the knot's centroid; $r$, the radial distance from the pulsar in ($0\rlap{.}''05$) pixels.

pulsar, opposite but along the true pulsar–knot direction, and at an angular distance comparable to that of the true knot. We repeated the exercise by varying the flux, position, and morphology of the synthetic knot and we estimated the uncertainties in the parameters recovered using SExtractor.[14]

Table 10 lists the best-fit values of the model parameters of the inner knot for each of the first 17 observations based upon this traditional analysis and modeling. Table 11 shows the results of a regression analysis on the listed parameters. We obtained an additional five *HST* observations but did not perform the traditional analysis on those data.

---

[14] http://www.astromatic.net/software/sextractor

### A.2.2. HST-SVD

As the inner knot is within $1''$ of the Crab pulsar and varies in position and size, we also developed special procedures for characterizing it using the central $121 \times 121$ pixel ($6\rlap{.}''05 \times 6\rlap{.}''05$) images of the 22 *HST*/ACS observations. The major steps are (1) to remove the pulsar from each image, (2) to use the residual image to generate an image of the inner knot, and (3) to characterize the properties of the inner knot.

#### A.2.2.1. Remove the Pulsar and Generate an Image

In order to remove the pulsar from each of the 22 central $121 \times 121$ pixel ($6\rlap{.}''05 \times 6\rlap{.}''05$) *HST* images, we first
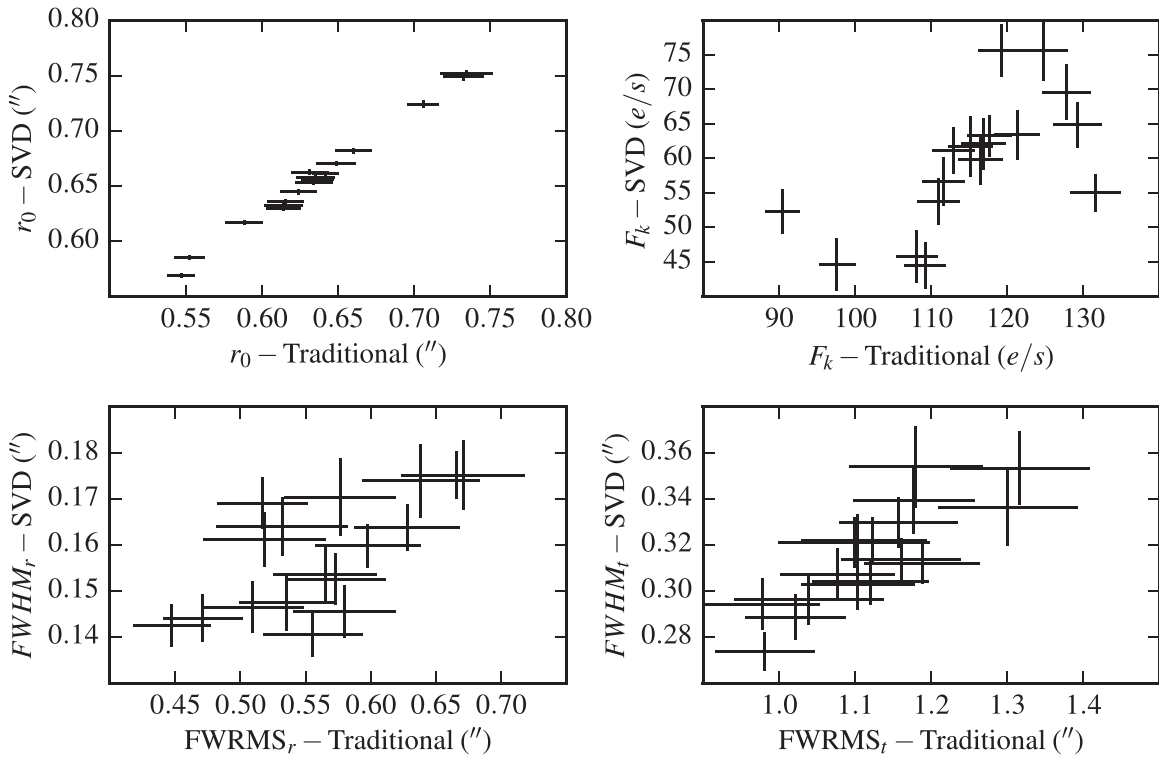
**Figure 15.** Comparison of *HST*-SVD and *HST*-traditional measured properties of the inner knot.

determine the PSF of the *HST*/ACS using $121 \times 121$ pixel images around each of the 19 isolated stars in the field. In doing this, we account for the fact that some observations were at a roll angle $\sim 180°$ opposite that of the others. After subtracting a fitted linear gradient from the image of each (Figure 12) of the 19 stars and for each of the 22 observations, we register the resulting $418 = 19 \times 22$ star images and use SVD to generate a linear basis (lowest term shown in Figure 12) describing the PSF. The model pulsar image (Figure 12) uses the first 72 components of the SVD basis. After subtracting a linear gradient from each of the 22 central (pulsar) images (Figure 13), we fit each using the PSF basis to generate 22 residual (pulsar removed) images (also Figure 13), each now dominated by the inner knot.

### A.2.2.2. Characterize Inner-knot Properties

The measured extrinsic properties of the inner knot are the projected radial separation $r_0$ and the polar angle $\psi_0$ of the peak surface brightness with respect to the pulsar. To facilitate characterization of the intrinsic properties of the inner knot, we map each inner knot sub-image (Figure 13) onto a $\psi$–$r$ grid (Figure 14). For an initial model of the surface brightness (intensity) distribution of the inner knot, we use a simple bivariate normal distribution: $S(r, \psi) = S_k \exp(-\frac{1}{2}((r - r_0)^2/\sigma_r^2 + (\psi - \psi_0)^2/\sigma_\psi^2))$.

The major intrinsic properties of the inner knot are its radial dispersion $\sigma_r$ (FWHM$_r = 2.35\sigma_r$ for a Gaussian profile), azimuthal dispersion $\sigma_\psi$ (or tangential dispersion $\sigma_t = r_0\sigma_\psi$), and peak intensity (surface brightness) $S_k$. Integrating the intensity over a solid angle gives the flux $F_k = 2\pi\sigma_r\sigma_t S_k$. In fitting this model to the $\psi$–$r$ image of the inner knot, we include a constant-surface-brightness background $S_b$ as a model parameter.

While this simple model provides adequate estimates to characterize the primary properties of the knot (Table 6), as a check we also introduced a somewhat more complicated model to deal with minor asymmetries in the $\psi$–$r$ plane. In particular, we took the radial location and radial width to be weak functions of the azimuthal angle, which we expand as a Taylor series to second order: $r \approx r(\psi) \approx r_0 + r_0'(\psi - \psi_0) + \frac{1}{2}r_0''(\psi - \psi_0)^2$ and $\sigma_r \approx \sigma_r(\psi) \approx \sigma_{r_0} + \sigma_{r_0}'(\psi - \psi_0) + \frac{1}{2}\sigma_{r_0}''(\psi - \psi_0)^2$. However, the derivatives proved not to significantly alter the results.

### A.2.2.3. Comparison Between Methods

The comparison between methods and the reasons for somewhat emphasizing the SVD-based results considers the various measured parameters individually. Figure 15 compares measurements of similar variables between the two methods. From the figure we see that with the possible exception of the knot flux, both methods yield measurements that track each other apart from a scale factor. This leads to the result that the pulsar–knot separation determines all of the intrinsic properties of the knot.

Differences for $r_0$ are quite small, whereas the knot flux and size estimates differ by factors of $\approx 2$. We would expect differences in the size estimates, as the two analyses are using different measures of knot size—the first, FWRMS; the second, FWHM—that are not simply related for a non-Gaussian profile. That the fluxes differ is perhaps not so surprising, as its measurement is sensitive to the method of background subtraction and the impact of emission in the wings of the inner knot's profile. A significant difference between the two methods is the smaller uncertainty in $r_0$ afforded by the SVD approach, which removes those SVD components that represent noise, thus enhancing signal to noise.

*A.3.* Chandra

Figure 6 shows the summed image at pulse minimum from the six "flaring" observations (ObsIDs 14684-16247 in Table 3). Prior to the binning used to produce the figure, we extract the counts in the three regions shown. It is difficult, if not impossible, to make use of the absolute number of counts as the different instrument configurations are all uncalibrated. However, we can make use of the relative numbers of counts from the different regions. Thus, the central region serves as an indicator of the number of pulsar counts, which can then be compared with the other observations to derive physical fluxes (assuming of course that the phase-averaged pulsar flux has not varied). The region to the southeast provides the upper limit for the flux in the knot and we use the region to the northwest to estimate the background, comprised mainly of that due to the wings of the pulsar PSF.

The alert reader will notice a slight excess of counts roughly $0\rlap{.}''6$ to the southwest of the pulsar. This feature is seen both in the phase-averaged pulse and in the data from ObsID 11245. (The asymmetric effect of the blade inserted for ObsID 9765 does not allow these data to be used in making this comparison.) Therefore, we conclude that this feature is part of the pulsar PSF. A more subtle effect is also present as there is a slight asymmetry in the PSF that causes the region we associate with the inner knot to be somewhat brighter than the background during observations taken in the fall. In the spring, when the spacecraft has (naturally) been set at a roll angle that differs by $\approx 180^\circ$ from that in the fall, the background region is brighter than that we associate with the location of the inner knot. This effect is mainly seen in the phase-averaged data, and by comparing data from the ObsID 9765 (spring) and ObsID 11245 (fall) observations. Both effects described in this paragraph are relatively minor and are mainly due to the fact that we are working slightly below the spatial resolution of *Chandra*; thus, these effects have been ignored in setting the upper limits in Table 8.

## REFERENCES

Aliu, E., Archambault, S., Aune, T., et al. 2014, ApJL, 781, LL11
Arons, J. 2012, SSRv, 173, 341
Baty, H., Petri, J., & Zenitani, S. 2013, MNRAS, 436, L20
Beckwith, S. V. W., Stiavelli, M., Koekemoer, A. M., et al. 2006, AJ, 132, 1729
Bertin, E., & Arnouts, S. 1996, A&AS, 117, 393
Bogovalov, S. V. 1999, A&A, 349, 1017
Buehler, R., Scargle, J. D., Blandford, R. D., et al. 2012, ApJ, 749, 26
Bühler, R., & Blandford, R. 2014, RPPh, 77, 066901
Buson, S., Buehler, R., & Hays, E. 2013, ATel, 5485, 1
Bykov, A. M., Pavlov, G. G., Artemyev, A. V., & Uvarov, Y. A. 2012, MNRAS, 421, L67
Camus, N. F., Komissarov, S. S., Bucciantini, N., & Hughes, P. A. 2009, MNRAS, 400, 1241
Cerutti, B., Uzdensky, D. A., & Begelman, M. C. 2012, ApJ, 746, 148
Cerutti, B., Werner, G. R., Uzdensky, D. A., & Begelman, M. C. 2013, ApJ, 770, 147
Clausen-Brown, E., & Lyutikov, M. 2012, MNRAS, 426, 1374
Fitzpatrick, E. L. 1999, PASP, 111, 63
Fruchter, A. S., & Hook, R. N. 2002, PASP, 114, 144
Ghez, A. M., Salim, S., Weinberg, N. N., et al. 2008, ApJ, 689, 1044
H. E. S. S. Collaboration Abramowski, A., Aharonian, F., et al. 2014, A&A, 562, A145
Hester, J. J. 2008, ARA&A, 46, 127
Hester, J. J., Scowen, P. A., Sankrit, R., et al. 1995, ApJ, 448, 240
Komissarov, S. S., & Lyubarsky, Y. E. 2003, MNRAS, 344, L93
Komissarov, S. S., & Lyutikov, M. 2011, MNRAS, 414, 2017
Kron, R. G. 1980, ApJS, 43, 305
Lyubarsky, Y. E. 2012, MNRAS, 427, 1497
Lyutikov, M., Balsara, D., & Matthews, C. 2012, MNRAS, 422, 3118
Lyutikov, M., Pariev, V. I., & Blandford, R. D. 2003, ApJ, 597, 998
Mayer, M., Buehler, R., Hays, E., et al. 2013, ApJL, 775, L37
Melatos, A., Scheltus, D., Whiting, M. T., et al. 2005, ApJ, 633, 931
Moran, P., Shearer, A., Mignani, R. P., et al. 2013, MNRAS, 433, 2564
Ng, C.-Y., & Romani, R. W. 2008, ApJ, 673, 411
Ojha, R., Hays, E., Buehler, R., & Dutka, M. 2013, ATel, 4855, 1
Porth, O., Komissarov, S. S., & Keppens, R. 2014, MNRAS, 438, 278
Rees, M. J., & Gunn, J. E. 1974, MNRAS, 167, 1
Sandberg, A., & Sollerman, J. 2009, A&A, 504, 525
Sollerman, J. 2003, A&A, 406, 639
Sollerman, J., Lundqvist, P., Lindler, D., et al. 2000, ApJ, 537, 861
Striani, E., Tavani, M., Piano, G., et al. 2011, ApJL, 741, L5
Sturrock, P., & Aschwanden, M. J. 2012, ApJL, 751, L32
Tavani, M., Bulgarelli, A., Vittorini, V., et al. 2011, Sci, 331, 736
Tchekhovskoy, A., Philippov, A., & Spitkovsky, A. 2015, arXiv:1503.01467
Tchekhovskoy, A., Spitkovsky, A., & Li, J. G. 2013, MNRAS, 435, L1
Tennant, A. F., Becker, W., Juda, M., et al. 2001, ApJL, 554, L173
Teraki, Y., & Takahara, F. 2013, ApJ, 763, 131
Tziamtzis, A., Lundqvist, P., & Djupvik, A. A. 2009, A&A, 508, 221
Uzdensky, D. A., Cerutti, B., & Begelman, M. C. 2011, ApJL, 737, L40
Weisskopf, M. C., Tennant, A. F., Arons, J., et al. 2013, ApJ, 765, 56
Wizinowich, P. L., Le Mignant, D., Bouchez, A. H., et al. 2006, PASP, 118, 297
Yelda, S., Lu, J. R., Ghez, A. M., et al. 2010, ApJ, 725, 331
Yuan, Q., Yin, P.-F., Wu, X.-F., et al. 2011, ApJL, 730, L15